Materials Today Bio 32 (2025) 101739

Contents lists available at ScienceDirect

Materials Today Bio

journal homepage: www.journals.elsevier.com/materials-today-bio

Multifunctional dual-layer microneedles loaded with selenium-doped carbon quantum dots and Astilbin for ameliorating diabetic wound healing

Zhen Zhang [a,1], Yulin Zhang [a,1], Liang Peng [b], Yi Xing [a], Xinru Zhou [a], Shuo Zheng [a], Yanli Zhang [a,*], Longquan Shao [a,**]

[a] Stomatological Hospital, School of Stomatology, Southern Medical University, Guangzhou, 510280, China
[b] The First People's Hospital of Guiyang, Guiyang, 550002, China

ARTICLE INFO

Keywords:
Microneedles
Selenium-doped carbon quantum dots
Nanoparticle
Diabetic wound
Angiogenesis

ABSTRACT

Diabetic wounds (DW) represent a significant clinical challenge due to chronic inflammation, excessive oxidative stress, and impaired angiogenesis, all of which hinder effective tissue regeneration. Existing drug delivery systems often fail to achieve sustained and targeted therapeutic efficacy. In this study, we developed a novel dissolvable dual-layer methacrylated gelatin (GelMA) microneedle (MN) co-loading selenium-doped carbon quantum dots (Se-CQDs) and Astilbin (AST) for enhanced DW treatment. The outer layer, enriched with Se-CQDs, rapidly scavenges reactive oxygen species (ROS), effectively alleviating oxidative stress at the wound site. Sequentially, the inner layer releases AST, exerting potent anti-inflammatory and pro-angiogenic effects. Preliminary findings suggest these effects may involve the modulation of cytoskeletal dynamics and peroxisome function, contributing to endothelial cell migration and angiogenesis. This controlled, sequential release MN establishes a low-oxidative, anti-inflammatory microenvironment, thereby promoting angiogenesis and accelerating wound repair. The pioneering integration of selenium-doped quantum dots and AST-loaded hydrogels offers a synergistic therapeutic strategy, setting a new standard for advanced diabetic wound care with substantial clinical promise.

1. Introduction

Diabetes mellitus is a serious metabolic disorder that profoundly impacts patient prognosis and quality of life through its chronic complications. Among these, impaired wound healing, particularly diabetic foot ulcer (DFU), is widely recognized as one of the most devastating and disabling consequences of diabetes. By 2030, the global prevalence of diabetes among adults is estimated to rise to 7.7 %, epidemiological studies have shown that approximately 15–25 % of diabetic patients will develop a foot ulcer during their lifetime, with up to 24 % of cases eventually progressing to lower limb amputation, posing a significant threat to patient survival and well-being [1,2,3,4]. Diabetic wounds (DW) exhibit significantly impaired healing capabilities due to complex pathological features, including chronic inflammation, oxidative stress, and angiogenesis dysfunction, leading to a substantially prolonged healing process [5,6,7].

Persistent hyperglycemia not only escalates reactive oxygen species (ROS) production but also perpetually activates M1 macrophages, intensifying chronic inflammation and inhibiting angiogenesis [8,9,10,11]. These pathophysiological mechanisms not only obstruct normal tissue repair but also markedly increase infection risk, further complicating wound healing [5]. Existing therapeutic approaches, including glycemic control, topical antibiotics, and debridement, while alleviating symptoms, fail to adequately address the deep-seated issues of excessive ROS and chronic inflammation [12,13].

Recent advances in wound dressing technologies have employed nanomaterials, engineered scaffolds, and hydrogels for drug delivery and sustained release [14,15,16]. However, physical barriers such as the skin and scar tissue formed during the healing process limit the effectiveness of these interventions in delivering therapeutics deep into the wound site [17,18,19]. Microneedle (MN) technology, penetrating the skin barrier and delivering drugs directly to the wound bed, significantly enhances drug bioavailability and therapeutic outcomes, emerging as a promising strategy for DW management [20,21,22].

* Corresponding author.
** Corresponding author.
E-mail addresses: 541292702@qq.com (Y. Zhang), shaolongquan@smu.edu.cn (L. Shao).
[1] These authors contributed equally to this work.

https://doi.org/10.1016/j.mtbio.2025.101739
Received 23 January 2025; Received in revised form 2 April 2025; Accepted 6 April 2025
Available online 10 April 2025

As shown in Scheme 1, we developed a dual-layer methacrylate gelatin (GelMA) MN system targeting multiple pathological features of DW, including oxidative stress, chronic inflammation, and angiogenesis impairment [23]. The MN backing, composed of polyvinyl alcohol (PVA), provides robust mechanical support, ensuring structural integrity upon insertion [24]. The needle tips, fabricated using GelMA hydrogel, offer biocompatibility and controlled degradation properties, suitable for efficient drug loading and release [25,26]. Astilbin (AST), a naturally occurring flavonoid widely present in various plants, has garnered significant attention in recent years for its potent anti-inflammatory and pro-angiogenic properties. Existing studies have demonstrated the remarkable efficacy of AST in treating conditions such as diabetic nephropathy, diabetes mellitus and burn wounds [27,28,29]. *In vitro* research has further confirmed that AST promotes endothelial cell migration and angiogenesis by activating the PI3K/Akt and ERK1/2 signaling pathways [30]. Therefore, AST holds great potential for

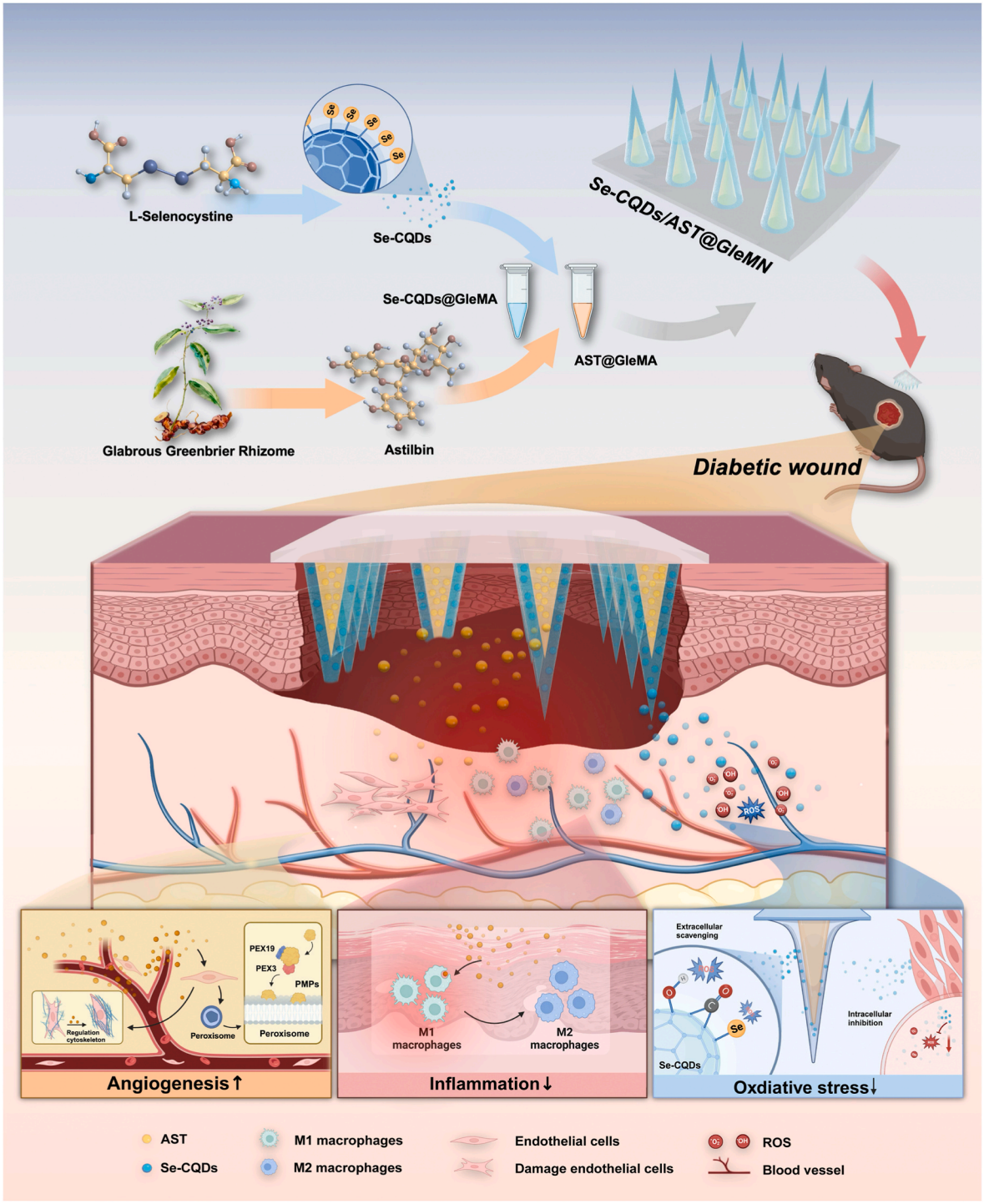

Scheme 1. Design and Mechanism of Se-CQDs/AST@GelMA Microneedles for Diabetic Wound Healing. The schematic illustrates the dual-layer microneedle design, with Se-CQDs in the outer layer and AST in the inner layer. Se-CQDs, synthesized from L-Selenocystine, target ROS, reducing oxidative stress upon release. The inner layer containing AST, extracted from Glabrous Greenbrier Rhizome, is released subsequently to induce M2 macrophage polarization and enhance angiogenesis, collectively promoting diabetic wound healing.

application in the treatment of DW healing. We explored the molecular mechanisms of AST in modulating macrophage polarization and endothelial cell function through both *in vitro* and *in vivo* experiments. AST was incorporated into the inner layer of a MN system to leverage its significant anti-inflammatory and pro-angiogenic effects. To address the excessive production of ROS in DW, the outer layer of the MN system was loaded with Selenium-doped Carbon Quantum Dots (Se-CQDs) [31]. The introduction of selenium significantly enhanced the antioxidant properties of CQDs, enabling effective ROS scavenging within the wound microenvironment while maintaining excellent biocompatibility and reducing oxidative stress-induced cellular damage [32].

This dual-layer MN system offers a synergistic therapeutic approach by combining AST's anti-inflammatory and pro-angiogenic effects with the strong antioxidant properties of Se-CQDs. AST modulates the immune response, promotes tissue repair, and enhances angiogenesis, while Se-CQDs efficiently clear ROS and mitigate oxidative stress-induced damage. The combined action of these components significantly improves the wound microenvironment, accelerating the healing process. *In vivo* experiments revealed that the dual-layer MN system substantially shortened the healing time of DW, reduced inflammation, and promoted angiogenesis and tissue regeneration. These results suggest that this system holds great therapeutic potential, offering a novel strategy for the clinical treatment of DW.

2. Materials and methods

2.1. Materials

All experimental materials and reagents were sourced from commercial vendors. L-Selenocystine was obtained from Shanghai Macklin Biochemical Co., Ltd. (Macklin, S838591, China), while AST was supplied by MCE Co. (US). GelMA and PVA were procured from Yongqinquan Intelligent Equipment Co., Ltd. (EFL, EFL-GM-60, EFL-PVA-001, China).

2.2. Preparation and characterization of Se-CQDs

L-Selenocystine (200 mg) was melted in 10 mL of ultrapure water, and the pH was changed to 9. The solution was stirred and heated at 60 °C until fully dissolved, then transferred to a high-temperature, high-pressure reactor to react for 24 h. Afterward, the reaction mixture was centrifuged at 12,000 g for approximately 10 min using a high-speed centrifuge (Thermal, ST16R, China). The brown supernatant was collected and dialyzed (MWCO 500 Da) before being freeze-dried using a lyophilizer (CoolSafe, 110-4, China) for 24 h to obtain Se-CQDs powder for further experiments.

The Se-CQDs were characterized using various methods. Transmission Electron Microscopy (TEM, Talos, F200S G2 S/TEM, US) was used to examine their morphology and particle size, with ImageJ employed to calculate the average particle size. Thickness measurements were conducted using Atomic Force Microscopy (AFM, Bruker, Dimension Edge, DE). Dynamic light scattering (DLS, Malvern, ZEN3600, UK) was used to determine the hydrodynamic diameter and zeta potential. Fourier Transform Infrared Spectroscopy (FT-IR, Bruker, TENSOR27, DE) was utilized for molecular structure analysis, while X-ray Photoelectron Spectroscopy (XPS, Thermo, K-Alpha, US) was conducted to assess the element composition and chemical chemical structure. The antioxidant activity of Se-CQDs was determined via electron spin resonance spectroscopy (Bruker, A300 EMXplus, DE). Ultraviolet–visible (UV–Vis) spectroscopy (Shimadzu, UV-2501 PC, Japan) was utilized to document the UV–Vis absorption spectrum.

The antioxidant status of skin tissue was assessed by measuring the levels of superoxide dismutase (SOD), MDA, and CAT using assay kits (Beyotime, S0051, China). For SOD analysis, tissue homogenates were centrifuged at 10,000 g for 5 min at 4 °C, and the resulting supernatants were incubated with WST and enzyme reagents at 37 °C for 20 min. Absorbance was measured at 450 nm using a microplate reader (SpectraMax, 190, US). Malondialdehyde (MDA) levels were determined by mixing supernatants with MDA working solution, boiling at 100 °C for 15 min, followed by absorbance measurement at 532 nm. To assess catalase (CAT) activity, supernatants were mixed with CAT assay buffer and 250 mM H_2O_2, followed by incubation at room temperature for 5 min. Absorbance was then recorded at 240 nm. All results were calculated according to the manufacturer's protocols.

2.3. Preparation and characterization of GelMN

A 500 μL solution of GelMA (10 % w/v, EFL, EFL-GM-60, Suzhou, China) was prepared and filled into the grooves of a pre-fabricated polydimethylsiloxane (PDMS) MN mold. The solution was then photo-crosslinked by exposing it to 405 nm ultraviolet light for 5 min with a vacuum pump (Zhejiang Value Mechanical & Electrical Products, Y605, China), forming the MN tips. The backing layer was formed by curing PVA at 37 °C for 24 h. The microneedles' structure was examined with a fluorescence stereo microscope (AxioZoom V16, DE) for visualization purposes. The surface of the Se-CQDs was analyzed with a scanning electron microscope (SEM, Carl Zeiss, Sigma 300, DE), complementing the morphological analysis conducted by TEM and AFM.

2.4. Preparation and characterization of Se-CQDs/AST@GelMN

The Se-CQDs/AST@GelMN (S/A@GelMN) dual-layer microneedles were fabricated using a two-step method. First, solutions of 10 % w/v GelMA were prepared, dissolving Se-CQDs and AST separately to form Se-CQDs@GelMA (1000 μg/mL) and AST@GelMA (1000 μM) solutions. The Se-CQDs@GelMA solution was filled into the PDMS MN mold, and a vacuum pump was used to remove air bubbles. A 3 μm metal spacer was applied to control the thickness of the outer MN layer, and an MN protruding mold was used to remove any excess solution. The mold was then exposed to 405 nm UV light for 5 min to photo-crosslink the solution, forming the outer MN layer. Next, the remaining space in the PDMS mold was filled with the AST@GelMA solution, and the same procedure was repeated to fabricate the inner MN layer. The structure of the microneedles was analyzed and observed using a SEM. To visualize the dual-layer structure, GelMA was fluorescently labeled with fluorescein isothiocyanate (FITC) and rhodamine B (RB), creating FITC/RB@GelMN. The dual-layer structure was then imaged using a fluorescence stereo microscope (Carl Zeiss, AxioZoom V16, DE).

2.5. Mechanical properties of the MN

The mechanical strength of S/A@GelMN was evaluated using a Series Universal Testing System (Instron, 3366, US). MN were positioned with tips facing upward on the testing platform, and a texture analyzer probe was lowered at 0.02 mm/s until contacting the needle tip. The applied force was continuously monitored, generating a force-displacement curve. To evaluate the skin penetration efficiency of S/A@GelMN, both *in vivo* and *ex vivo* studies were conducted. For *in vivo* testing, mice were anesthetized using isoflurane, and the dorsal skin was shaved and depilated. The microneedle patch was applied to the dorsal skin with gentle pressure for either 10 s or 3 min. Subsequently, the microneedle patch was removed, and the skin surface was photographed to assess residual imprint and dissolution behavior. Skin tissue from the application site was collected for histological evaluation, then fixed in 4 % paraformaldehyde, paraffin-embedded, sectioned, and stained with hematoxylin and eosin (H&E). Cross-sectional images were obtained to examine the depth and completeness of microneedle insertion. For *ex vivo* testing, freshly excised mouse dorsal skin was mounted on a supporting surface and treated with the microneedle patch under identical conditions (10 s or 3 min). The skin surface was subsequently photographed to observe microneedle imprint clarity and residual material.

2.6. Degradation and drug release of MN

The *in vitro* biodegradation of GelMN was assessed in PBS solution (Gibco, C10010500BT, US). GelMN samples were immersed in PBS, and wet weights were recorded every two days for 14 days to monitor changes and plot the swelling profile. For drug release analysis, FITC-labeled Se-CQDs were incorporated into GelMA, forming FITC-Se-CQDs@GelMN. The samples were immersed in PBS, and fluorescence images were obtained with a fluorescence stereo microscope to track fluorescence signals over time. Supernatants were collected at two-day intervals, and fluorescence was quantified using a microplate reader (BMG, CLARIO-star, DE). To evaluate AST release, AST was embedded into GelMA to form AST@GelMN, which was then incubated in PBS at 37 °C. Supernatants were collected every 24 h, and AST concentrations were measured employing high-performance liquid chromatography (HPLC) to analyze the release profile.

2.7. Cell culture

HUVECs and RAW264.7 cells were sourced from Procell (Procell, PUMC-HUVEC-T1, China). HUVECs were cultured in DMEM complete medium, consisting of DMEM (Gibco, 11965092, US) supplemented with 10 % FBS (Procell, 164210-50, China) and 1 % penicillin-streptomycin solution (Gibco, 15070063, US). RAW264.7 cells were cultured in RPMI 1640 complete medium, prepared with Roswell Park Memorial Institute 1640 medium (Gibco, 15070063, US) and supplemented with 10 % FBS.

2.8. Cell proliferation and viability assay

The MTT assay was chosen for testing cell viability in the experiment. HUVECs were cultured in 96-well plates and maintained at 37 °C for a 24-h incubation period. Cells were then treated with Se-CQDs at various concentrations (1 μg/mL to 250 μg/mL) for 12 h, with five replicates per group. After treatment, 5 mg/mL MTT could added and incubated for almost 4 h. Following incubation, to solubilize the formazan, 150 μL of DMSO (SIGMA, D2650-100ml, US) was added to each well, and the plate was agitated for 10 min. Absorbance was measured at 490 nm. The same protocol was used to detect the effect of AST (20–80 mM) on HUVECs and RAW264.7 cells over 12 h. To analyze the effect of Se-CQDs on the cell cycle, HUVECs were treated with 25, 50, 100, and 200 μg/mL of Se-CQDs for 12 h. After treatment, 5×10^5 cells were collected with EDTA-free trypsin, washed with specialized cleaning agent, treated with RNase A reagent, for 30–45 min. Then, cells cultured with Propidium iodide (PI) in an environment without light. for almost 30 min. Finally, cells were analyzed by flow cytometry (Beckman, CytoFLEX S, US) to measure red fluorescence at 488 nm.

2.9. Antioxidant activity of Se-CQDs

Se-CQDs solutions were prepared at diversified concentrations (25, 50, 100, and 200 μg/mL). The ABTS radical scavenging ability was measured using the Total Antioxidant Capacity (T-AOC) Colorimetric Assay Kit (Elabscience, E-BC-K219-M, China). Hydroxyl radical removal, DPPH scavenging, and superoxide anion (O2·-) scavenging were checked with detection kits, separately (H931091-50 T/EA, MACKLIN, China), (Elabscience, E-BC-K807-M, China), and (Elabscience, E-BC-K001-M, China). To assess the impact of Se-CQDs on intracellular ROS levels in HUVECs, the DCFH-DA ROS probe (Solarbio, D6470, China) was used. HUVECs were treated with Se-CQDs for 12 h. Experimental groups included a blank control, a high glucose (HG) group (HUVECs treated with HG for 24 h), and a Se-CQDs group (HG and 25–200 μg/mL Se-CQDs). DCFH-DA fluorescence intensity stands for ROS level within HUVECs, which was recorded by confocal laser scanning microscopy (CLSM, Leica, STELLARIS 5, DE).

2.10. AST-induced macrophage polarization

RAW246.7 cells in a 6-well plate were divided into three groups: control, LPS, and AST. Both LPS and AST groups were treated with 1 mg/mL LPS (MERCK, L2880, DE) for 12 h, while the AST group additionally received 30 mM AST treatment for 12 h. For flow cytometry, cells were incubated with CD86-FITC (105005, Biolegend, US) or CD206-APC750 (Biolegend, 141708, US) antibodies for 30 min before analysis. Immunofluorescence (IF) staining was conducted using CD86 (Affinity, DF6332, China) and CD206 (Abcam, ab300621, US) antibodies, and fluorescence images were captured using CLSM.

2.11. Cell scratch assay

HUVECs were incubated in 60 mM HG DMEM for 48 h, followed by 30 mM AST treatment for 12 h. Cells were divided into control, HG, and AST groups. Once cell confluency reached 95%, cell monolayers were scratched using a 200 μL pipette tip to simulate a wound. Following a 12-h culture in serum-free DMEM, cell migration was then imaged using a microscope (Olympus, IX73, Japan).

2.12. Transwell assay

HUVECs were divided into control, HG, and AST groups following the treatments described earlier. Cells in serum-free DMEM were placed in the upper chamber of a Transwell insert (Corning, 3422, US), with 2 % FBS medium in the lower chamber. Cells were fixed with cell fixative and stained with crystal violet (Beyotime, C0121, China). Migration was imaged using a fluorescence stereo microscope and measured with ImageJ software.

2.13. Tube formation assay

HUVECs were divided into control, HG, and AST groups and pre-treated as described. A total of 100 μL of Matrigel (BD, 356237BD, US) was added to 96-well plates and incubated for a period of 30 min to solidify. Pre-treated cells were then resuspended in serum-free DMEM and seeded onto the Matrigel at a density of 5×10^4 cells per well. Images were taken at 6 and 12 h using a microscope (Olympus, IX73, Japan), and tubular structures were analyzed using ImageJ with the angiogenesis plugin.

2.14. Western blotting

HUVECs were treated with HG for 48 h, followed by co-incubation with AST at concentrations of 10, 20, 30, and 40 mM. According to the provided protocol, total protein was obtained from tissue and cellular samples. Following SDS-PAGE separation, samples were transferred onto PVDF membranes (Millipore, IPVH 00010, USA) and incubated in Quickblot blocking buffer (Biotime, P0252, China). The primary antibodies used were GAPDH (Affinity, AF7021, China), CD31 (SantaCruz, sc-20071, US), VEGF (SantaCruz, sc-53463, US), RhoA (SantaCruz, sc-418, US), Cdc42 (SantaCruz, sc-8401, US), Actin (Affinity, DF3163, China), PEX19 (Affinity, DF4281, China), and PEX3 (Affinity, DF4282, China). Secondary antibodies included HRP-conjugated Goat Anti-Rabbit IgG (H + L) (Affinity, S0001, China) and Goat Anti-Mouse IgG (H + L) (Affinity, S0002, China). Signal detection was performed using SuperEnhanced ECL (GBCBIO, G3308, China), visualization was done with an automatic chemiluminescence imaging system (Tanon, Tanon 5200, China), and analyzed using ImageJ software.

2.15. RNA sequencing analysis

Following 48 h of high glucose (HG) exposure and 12 h of 30 mM AST pre-treatment, HUVECs were allocated into HG and AST groups for transcriptomic profiling. Total RNA was isolated using Trizol reagent

(Genesand, RE702, China). RNA sequencing was conducted using the DNBSEQ-T7 platform (MGI Tech, China). Data visualization and analysis were performed using R and Python tools.

2.16. Cytoskeleton staining

HUVECs were cultured on glass coverslips compatible with 24-well plates. After allowing cells to adhere, HG were added for 48 h, followed by incubation with 30 mM AST for 12 h. Cells were then fixed with cell fixative, stained with rhodamine-phalloidin (Solarbio, CA1610, China) to visualize the cytoskeleton, and counterstained with DAPI (Solarbio, S2110, China). Cytoskeletal organization and cellular morphology were analyzed using CLSM.

2.17. DW animal model construction

Eight-week-old male C57BL mice (weighing 20–25 g) were acquired from the Southern Medical University Animal Center (Guangdong, China). The institutional Animal Care and Use Committee approved all procedures involving animals in this study (approval number: IACUC-LAC-20240528-002). Following overnight fasting, mice housed under controlled conditions were intraperitoneally injected with 50 mg/kg STZ (Macklin, S6089, China). After anesthesia with isoflurane, hair was removed from the dorsal area, and an 8 mm full-thickness skin wound was created. Rubber rings were sutured around the wounds to maintain consistent contraction. Mice were divided into control (CTRL), Se-CQDs@GelMN (SMN), AST@GelMN (AMN), and Se-CQDs/AST@GelMN (S/AMN) groups.

2.18. In Vivo release study of GelMN

Se-CQDs were labeled with Cy5.5 (S1061, Solarbio, China) and incorporated into GelMA to create Cy5.5-Se-CQDs@GelMN and Cy5.5-Se-CQDs@GelMA (GM group). These were applied to DW mouse wounds, with subcutaneous injections of Cy5.5-labeled Se-CQDs as controls (ID group). On day 1 and day 4 post-application, tissue samples were collected, fixed in 4 % paraformaldehyde, and frozen using OCT compound (LEICA, FSC22, DE). Frozen sections were observed under CLSM. An *in vivo* imaging system (SINSAGE, IVIS-SII, China) monitored fluorescence in ID and GM groups from day 1 to day 14.

2.19. Wound healing assessment

Images of wounds from the CTRL, SMN, AMN, and S/AMN groups were captured on days 0, 7, and 14. Wound closure was quantified using ImageJ.

2.20. Histological analysis

Wound tissues were harvested on days 7 and 14 after euthanasia, followed by fixation, paraffin embedding, sectioning, and staining with H&E and Masson's trichrome. Staining intensity was quantified using ImageJ. For immunohistochemistry (IHC), CD31 (Affinity, AF6191, China) antibody was applied to detect neovascularization. Immunofluorescence (IF) analysis on day 14 used CD31 and 2 % Triton X-100 for permeabilization. Fluorescence images were captured using CLSM.

2.21. Statistical analysis

Data analysis was performed using GraphPad (Dotmatics, Version 10.2.3, US), and results were expressed as mean ± standard deviation (SD). For normally distributed data with homogeneity of variance, one-way ANOVA was applied to assess differences across multiple groups, followed by Tukey's multiple comparisons test to identify specific group differences. For experiments involving two independent variables, two-way ANOVA was used to evaluate the interaction effects between factors, with Tukey's multiple comparisons test applied where appropriate to compare differences between groups.

3. Results and discussion

One of the innovative aspects of this study is the development of a dual-layer GelMA MN (GelMN) system loaded with Se-CQDs and AST. Unlike traditional single-layer MN, the dual-layer design allows for a multi-target synergistic effect by incorporating different functional substances. This design maximizes the anti-inflammatory and pro-angiogenic effects of AST and the antioxidant properties of Se-CQDs through sequential release from the inner and outer layers. The dual-layer structure ensures gradual drug release, with the MN quickly penetrating the skin, dissolving, and releasing the drug. The outer layer of Se-CQDs is released first, rapidly scavenging excess ROS at the wound site, thus reducing oxidative stress and cell damage in a high-glucose environment. Subsequently, the inner layer releases AST, which inhibits inflammation and promotes angiogenesis, accelerating wound healing. Compared to conventional drug delivery systems, the dual-layer MN structure offers more precise and stable drug release, enhancing therapeutic efficacy [33,26]. This innovative design overcomes the limitations of traditional drug delivery methods, such as the inability to penetrate the skin barrier and inconsistent drug release, providing a more effective solution for treating DW.

3.1. Synthesis and characterization of Se-CQDs

In this study, GelMN system loaded with Se-CQDs and AST was designed and prepared. The Se-CQDs were synthesized as zero-dimensional nanomaterials targeting the excessive ROS microenvironment present in DW (Fig. 1a). During the synthesis, 200 mg of L-Selenocystine was used as a precursor, dissolved in 10 mL of ultrapure water, and corrected the pH value to 9. The solution was heated and stirred at 60 °C until fully dissolved, resulting in an orange-yellow solution. The reaction was carried out at 60 °C for 24 h. After completion, the solution was centrifuged at 12,000 g for 10 min, and the orange-yellow supernatant was collected, dialyzed for 3 days, and freeze-dried to obtain 15 mg of Se-CQDs, yielding approximately 7.5 %, consistent with previous reports [31].

The morphology and particle size distribution of Se-CQDs were characterized using TEM and AFM. TEM images clearly demonstrated the well-dispersed Se-CQDs, with particle sizes ranging from 1 to 5 nm (Fig. 1b). AFM results further revealed the uniformity in size and thickness, showing consistency with the TEM results (Fig. S1a). The mean hydrodynamic diameter of Se-CQDs was determined to be 31.095 nm using DLS measurements (Fig. 1c). The observed discrepancy between the hydrodynamic diameter from DLS and the physical size from TEM is attributed to the solvation layer and potential aggregation of Se-CQDs in aqueous solution, which increases the apparent size in DLS measurements. Accordingly, we further determined the average zeta potential of the Se-CQDs, which was −35.02 mV(Fig. 1d), indicating a substantial negative surface charge that contributes to the stability of the nanoparticles in aqueous solution and the formation of a pronounced solvation layer. In conjunction with the larger hydrodynamic diameter observed in DLS compared to the physical size in TEM, these findings corroborate the presence of a solvation layer on the particle surface and electrostatic repulsion between particles, resulting in an apparent increase in the measured particle size. Furthermore, the elemental composition, chemical states, and functional groups of Se-CQDs were thoroughly analyzed using XPS and FT-IR. FT-IR spectra (Fig. 1e) displayed characteristic absorption peaks for C=C, C-H, C-N, and C-Se bonds, confirming the structural integrity and presence of functional groups in Se-CQDs, which may play crucial roles in alleviating ROS [34,35]. Additionally, The XPS full spectrum confirmed the elemental composition of Se-CQDs, with a selenium content of 5.55 % by mass (Fig. 1f). The C1s spectrum showed different chemical states of carbon in

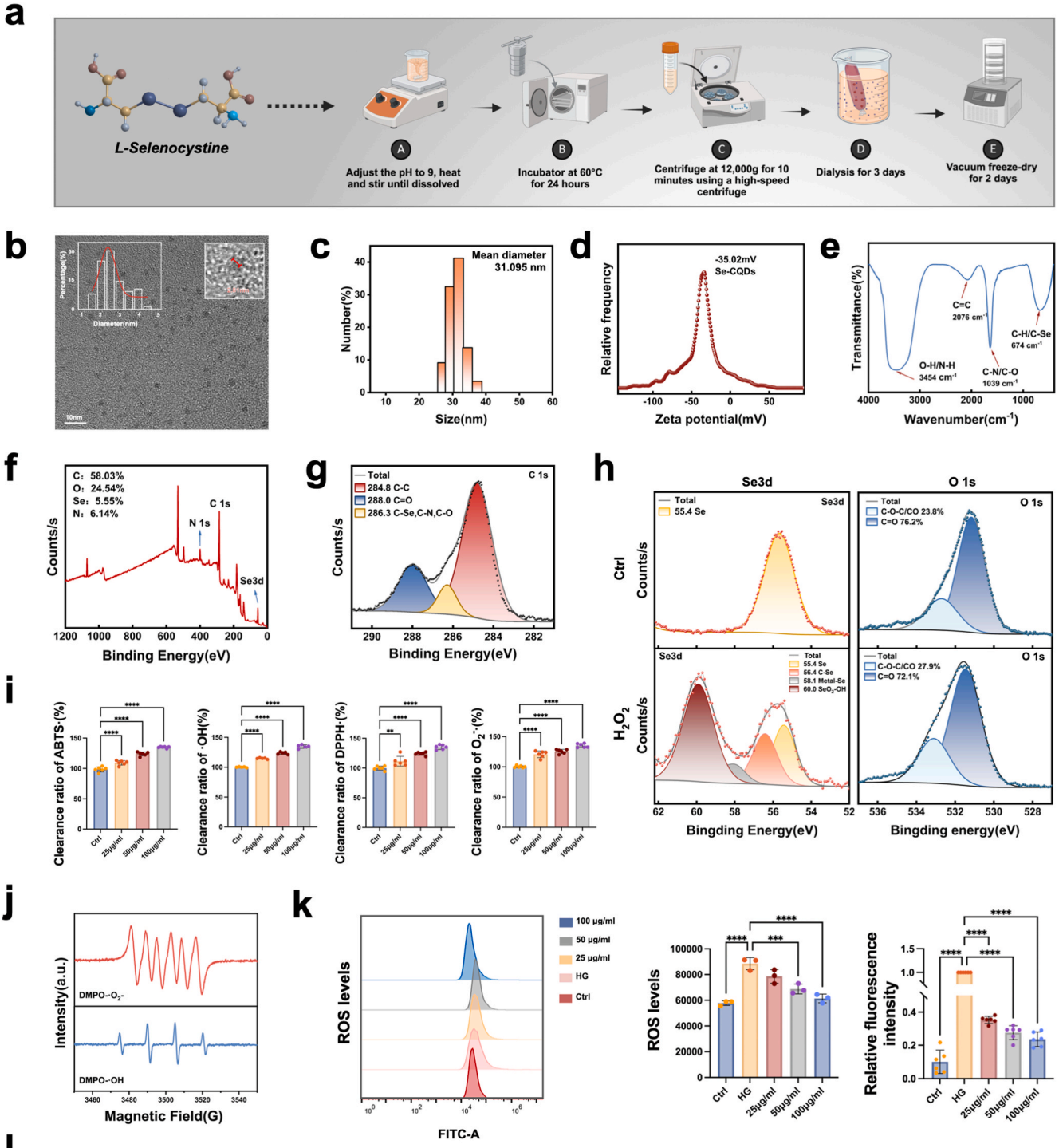

(caption on next page)

Fig. 1. Synthesis and Characterization of Se-CQDs (a) Schematic of Se-CQDs synthesis. (b) TEM image showing well-dispersed Se-CQDs. Inset: size distribution histogram and high-magnification image highlighting the spherical shape of individual Se-CQDs (c) DLS analysis showing a mean hydrodynamic diameter of 31.1 nm. (d) Zeta potential measurement indicating −35.02 mV. (e) FTIR spectrum showing functional groups (C=C, C-H, C-N, C-Se). (f) XPS survey spectrum indicating 5.55 % Se content. (g) High-resolution C 1s XPS spectrum showing C-C, C=O, and C-Se peaks. (h) XPS analysis of Se-CQDs before and after H_2O_2 treatment. Se3d and O1s spectra reveal oxidation of Se from Se^0 to higher oxidation states (SeO_2-OH) and an increase in C-O/C=O groups, confirming enhanced ROS scavenging capability. (i) ROS scavenging activity of Se-CQDs against $ABTS^{\cdot+}$, OH·, DPPH·, and $O_2^{\cdot-}$ radicals, demonstrating a dose-dependent increase in clearance ratios. (j) ESR spectra showing the scavenging activity of Se-CQDs against superoxide anion radicals ($O_2^{\cdot-}$) and hydroxyl radicals (·OH) in the presence of DMPO. (k) Flow cytometry analysis of ROS levels in HUVECs, showing a significant reduction in intracellular ROS following Se-CQDs treatment at various concentrations. (l) Confocal fluorescence images of HUVECs stained with DCFH-DA, demonstrating dose-dependent ROS reduction in cells treated with Se-CQDs (25, 50, and 100 μg/mL) under high-glucose (HG) conditions. The data are represented as mean ± SD (n = 5). *ns*: not significant, $^{**}P < 0.01$, $^{***}P < 0.001$, $^{****}P < 0.0001$.

Se-CQDs (Fig. 1g). The most intense binding energy peak at 284.8 eV confirmed the presence of sp2 carbon structure, alongside typical bonds such as C-C, C=O, and C-Se, indicating the successful incorporation of selenium into the CQD structure. Se3d spectra (Fig. S1b) further validated the covalent bonding of selenium in the CQDs. The ESR results demonstrated that Se-CQDs possess potent ROS scavenging capability (Fig. 1j). The characteristic signals of DMPO–·O_2^- and DMPO–·OH adducts were significantly suppressed following treatment with Se-CQDs. This indicates a marked reduction in both superoxide and hydroxyl radical levels, confirming that Se-CQDs can efficiently eliminate ROS *in vitro*. These findings support the antioxidative properties of Se-CQDs and highlight their potential for mitigating oxidative stress in biological environments. The optical properties of Se-CQDs were characterized using UV–Vis and fluorescence spectroscopy. The UV–Vis spectrum showed a distinct absorption peak at 290 nm, indicating strong UV absorption capability of Se-CQDs. Fluorescence spectra revealed a strong emission peak at 454 nm, highlighting the potential of Se-CQDs for applications in bioimaging (Fig. S1c).

3.2. ROS scavenging activity of Se-CQDs loaded in the outer layer

In diabetic patients, prolonged exposure to hyperglycemia and hypoxic conditions leads to excessive accumulation of ROS in DW. The outer layer of the S/A@GelMN system, loaded with Se-CQDs, demonstrates both excellent biocompatibility and effective ROS scavenging properties. Initially, the cytotoxicity of Se-CQDs was assessed by treating HUVECs with different concentrations (10 μg/mL to 250 μg/mL), using the MTT assay. The results indicated that Se-CQDs had low toxicity across this concentration range, with no significant difference in cell viability compared to the control group (Fig. S1g). Additionally, flow cytometry was performed to examine the effect of Se-CQDs on the cell cycle of HUVECs. In a HG environment, most cells were arrested in the G1 phase, indicating reduced proliferative capacity. However, treatment with Se-CQDs at concentrations between 10 μg/mL and 100 μg/mL showed no significant changes in cell cycle distribution across the G1, S, and G2/M phases, further demonstrating the biocompatibility of Se-CQDs (Fig. S3a).

To assess the ROS scavenging activity of Se-CQDs, we evaluated their ability to neutralize two representative ROS species: The Se-CQDs demonstrated broad-spectrum and potent scavenging activity against various ROS, including $ABTS^{\cdot+}$, OH·, DPPH·, and $O_2^{\cdot-}$, with a clear concentration-dependent trend. These results underscore the strong ROS-scavenging ability of Se-CQDs (Fig. 1i). To further elucidate the underlying antioxidant mechanism of Se-CQDs, we compared their XPS spectra before and after reaction with H_2O_2 (Fig. 3h). The Se3d spectra revealed that H_2O_2 treatment induced oxidation of selenium within Se-CQDs, partially converting elemental selenium into higher oxidation states, as indicated by the distinct SeO_2-OH peak. Additionally, the O1s spectra showed an increase in the proportion of C-O-C groups to 27.9 %, implying the generation of additional oxygen-containing moieties on the surface of CQDs. These findings confirm the strong ROS-scavenging capability of Se-CQDs.

Given this high ROS scavenging efficiency, we further investigated the intracellular ROS scavenging potential of Se-CQDs. ROS levels in HUVECs were measured using the fluorescent probe DCFH-DA. Confocal microscopy revealed a significant increase in ROS fluorescence intensity under HG conditions (Fig. 1k), while the intensity was markedly reduced in cells treated with Se-CQDs. Flow cytometry analysis further confirmed a concentration-dependent reduction in intracellular ROS fluorescence following Se-CQDs treatment (Fig. 1l). These results demonstrate that Se-CQDs exhibit excellent biocompatibility and effectively scavenge ROS, thereby reducing oxidative stress-induced damage in cells exposed to high glucose levels.

In vivo, biochemical analyses of skin tissue homogenates revealed that diabetes significantly impaired endogenous antioxidant defense (Figs. S1d–f). Specifically, the activity of SOD was markedly reduced in the diabetes group compared to the control group, while Se-CQDs treatment significantly restored SOD levels (Fig. S1d). In contrast, MDA, a key indicator of lipid peroxidation, was substantially elevated in the diabetic group, whereas Se-CQDs administration significantly decreased MDA levels (Fig. S1e). Furthermore, CAT activity, which was also suppressed in diabetic skin, was notably improved following Se-CQDs treatment (Fig. S1f). These findings confirm the *in vivo* antioxidant capacity of Se-CQDs and their potential to alleviate oxidative stress in diabetic wounds.

3.3. Preparation and characterization of Se-CQDs/AST@GleMN

Current DW dressings face challenges in penetrating the skin and scar tissues, making MN drug delivery systems a promising solution for overcoming these barriers. In this study, we fabricated the dual-layer MN system using a stepwise casting and UV curing technique (Fig. 2b). GelMA hydrogel, due to its excellent biocompatibility and tunable degradation, was chosen as the ideal drug-loading matrix. A 10 % w/v GelMA solution was prepared, degassed under vacuum to eliminate bubbles, and then cast into pre-fabricated polydimethylsiloxane (PDMS) MN molds (Fig. S2a). UV light (405 nm) was applied for 5 min to form the needle tips. Subsequently, PVA was selected as the backing layer to provide adequate mechanical support, ensuring the structural integrity of the microneedles during skin penetration. The resulting MN was a transparent, rigid structure arranged in a 15 × 15 array on a 13.5 mm square patch with evenly spaced needles (Fig. 2a). SEM revealed sharp, conical MN tips, approximately 600 μm in height, 120 μm in base diameter, and 25 μm at the tip (Fig. 2c).

Building on the GleMN fabrication, we produced dual-layer GelMN using a convex mold (Fig. 2b and S2a). A 10 % GelMA solution was mixed with 500 μg/mL Se-CQDs via ultrasonication for 5 min, degassed, and a 3 μm metal spacer was used to control the thickness of the outer MN layer. Excess liquid was removed using a convex mold, leaving space for the inner layer. After UV curing, the convex mold was removed, and a 10 % GelMA solution containing 1000 μM AST was poured into the remaining mold space to form the inner layer. The process was the same as for GelMA preparation [24,36,37]. SEM images confirmed the presence of Se-CQDs on the MN surface (Fig. 2c). To visualize the dual-layer structure, Rhodamine and FITC dyes were used to label Se-CQDs. The resulting double-layer hydrogel MN, with Rhodamine-labeled Se-CQDs in the outer layer and FITC-labeled Se-CQDs in the inner layer, was observed using a fluorescence stereo microscope, confirming successful fabrication of the dual-layer S/A@GelMN (Fig. 2d). Subsequently, FTIR spectroscopy was employed to characterize the chemical composition of

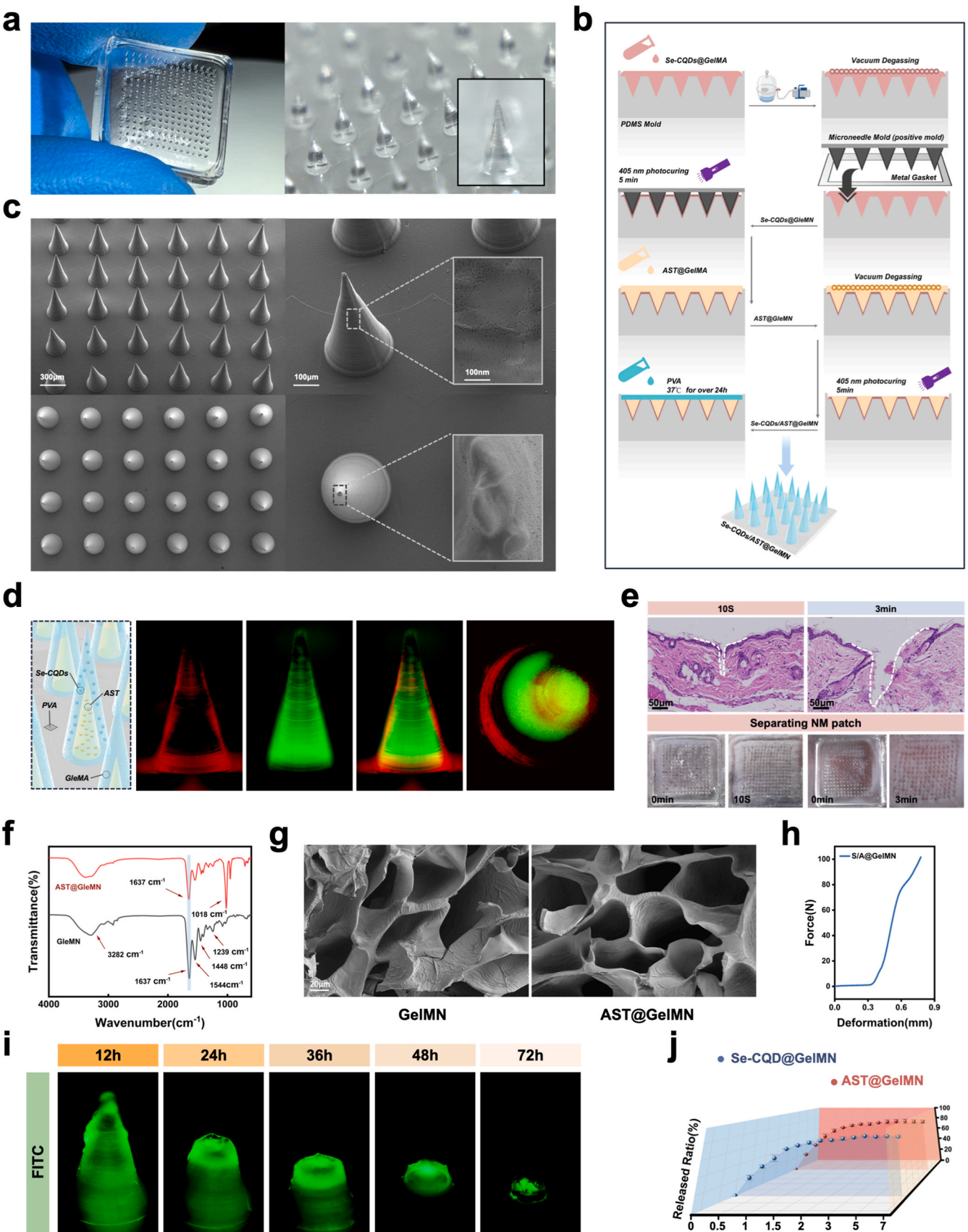

(caption on next page)

Fig. 2. Preparation and Characterization of Se-CQDs/AST@GleMN. (a) Photographs of S/A@GelMN microneedle array, showing a transparent, conical needle structure with a sharp tip (inset). (b) Schematic illustration of the fabrication process for dual-layer GelMN using stepwise casting and UV curing, forming an outer layer of Se-CQDs@GelMN and an inner layer of AST@GelMN. (c) SEM images of the microneedle array showing uniform, sharp needles with high aspect ratios. Insets highlight the smooth surface morphology. (d) Schematic representation of the dual-layer microneedle structure, Fluorescence images of the dual-layer microneedle labeled with FITC and Rhodamine. (e) Evaluation of microneedle insertion efficiency at different time intervals. (Top) H&E staining of skin sections after application of microneedles for 10 s and 3 min, respectively. Partial penetration was observed after 10 s, while complete insertion into the dermis was achieved after 3 min (Bottom) Photographs of the microneedle patches and skin surface before and after insertion. The microneedles began to detach from the patch base and insert into the skin as early as 10 s, while a 3-min application ensured full insertion and dissolution. (f) FT-IR spectra of GelMN and AST@GelMN, showing characteristic peaks confirming the successful incorporation of AST. (g) SEM images comparing the internal structure of GelMN and AST@GelMN, indicating no significant alteration in pore morphology after AST loading. (h) Mechanical strength test of S/A@GelMN, demonstrating sufficient force for skin penetration. (i) Time-lapse fluorescence images of FITC-labeled Se-CQDs release over 72 h in PBS, showing sustained release from the microneedles. (j) Cumulative release profiles of Se-CQDs and AST from GelMN, showing distinct release kinetics for the dual-layer system over 7 days.

GelMN and AST@GelMN, revealing a characteristic peak at 1018 cm^{-1} in AST@GelMN, confirming the successful loading of AST(Fig. 2f). Moreover, SEM analysis indicated that the incorporation of AST did not significantly alter the pore size, porosity, or wall thickness of the GelMN structure(Fig. 2g). To ensure the MN could penetrate the skin, mechanical testing demonstrated that Se-CQDs@GelMN and AST@GelMN could withstand a load of 100 N, sufficient to pierce the skin (Fig. 2h). Additionally, we tested the penetration of S/A@GelMN in mouse dorsal skin models, which showed 10-s application resulted in partial penetration into the skin layers, with incomplete disruption of the stratum corneum and limited delivery depth. In contrast, a 3-min application facilitated full insertion of the MN tips into the dermis, indicating more efficient delivery [38]. These findings are further supported by skin surface imaging, which shows clearer dissolution and imprint patterns after 3 min compared to 10 s (Fig. 2e). This difference may be attributed to factors such as the mechanical resistance of the skin, the viscoelastic properties of the GelMA matrix, and the gradual softening of the microneedle tips at body temperature. From a clinical translation perspective, these findings underscore the importance of optimizing application duration to ensure effective skin penetration and therapeutic efficacy. Unlike conventional injections, microneedles rely on a minimally invasive yet efficient delivery mechanism, which requires adequate insertion time to achieve reliable performance. In future clinical applications, personalized adjustment of application duration, particularly with consideration of individual differences in skin thickness and elasticity, may further enhance the clinical utility and therapeutic consistency of microneedle-based delivery systems.

Next, recognizing that DWs suffer from persistent ROS, inflammation, and impaired angiogenesis, we focused on the MN's sustained release properties, crucial for long-term wound healing. FITC-labeled Se-CQDs loaded in GelMN were tracked using a fluorescence stereo microscope over 72 h in phosphate-buffered saline (PBS). The MN gradually dissolved, with diminishing green fluorescence indicating continuous release of FITC@Se-CQDs (Fig. 2i). The release profiles of Se-CQDs@GelMN and AST@GelMN showed that the drug release rate stabilized after 2 days (Fig. 2j). Similarly, the MN swelling curve showed that 23.53 % of the MN weight remained after 2 days, consistent with the fluorescence images (Fig. S2b). These results demonstrate that the dual-layer structure of S/A@GleMN enables efficient skin penetration and rapid drug release [33,24].

3.4. *In vitro* polarization of macrophages and promotion of HUVECs angiogenesis by AST

In the dual-layer S/A@GelMN MN system, the outer layer releases Se-CQDs to efficiently scavenge excess ROS, followed by the rapid release of AST from the inner layer, which reduces inflammation, induces M2 macrophage polarization, and promotes angiogenesis in HUVECs. AST, a natural flavonoid extracted from the Glabrous Greenbrier Rhizome (Fig. 3a), was encapsulated in the inner layer of the dual-layer GelMA hydrogel MN system. Its sustained release to the wound site modulates macrophage polarization and endothelial cell function, ultimately promoting diabetic wound healing. To begin, RAW264.7 macrophages and HUVECs were selected as target cells to assess the biocompatibility of AST using the MTT assay. Results showed that AST concentrations below 60 mM had no significant effect on the viability of RAW264.7 or HUVECs, confirming AST's excellent biocompatibility (Fig. 3b). Macrophages are key regulators of immune responses and tissue repair during wound healing. During the healing process, M1 macrophages participate in pro-inflammatory responses, while M2 macrophages are involved in tissue repair. In DW, macrophages are predominantly polarized toward the M1 phenotype, with insufficient M2 macrophage presence, leading to chronic inflammation and delayed wound healing. Prior research has shown that AST modulates inflammatory cytokine production and reduces inflammatory responses. To validate AST's ability to induce M2 macrophage polarization, immunofluorescence staining was performed for CD86 (M1 marker) and CD206 (M2 marker). Fluorescence results showed (Fig. 3c) that LPS stimulation caused RAW264.7 macrophages to polarize toward the M1 phenotype, with an increase in CD86-positive cells. Conversely, AST significantly promoted M2 polarization, as evidenced by an increase in CD206-positive cells. Flow cytometry analysis further confirmed this, with CD206-positive cells increasing from 0.25 % to 0.15 % in the control and LPS groups, respectively, to 0.38 % after AST treatment (Fig. 3d).

Angiogenesis is also essential for the repair process in DW. Previous studies have demonstrated that AST facilitates neovascularization by activating the PI3K/Akt and ERK1/2 signaling pathways [30]. To investigate AST's effect on HUVECs under HG conditions, we optimized the glucose concentration for *in vitro* experiments. Scratch assays revealed that 60 mM glucose treatment for 48 h significantly reduced HUVEC angiogenesis (Fig. S4a) [39]. Western blot analysis further confirmed that 60 mM glucose treatment for 48 h reduced the expression of angiogenesis-related proteins CD31 and VEGF (Fig. S4b). Thus, 60 mM glucose for 48 h was selected as the HG condition for further experiments. Next, we explored the optimal concentration and treatment time for AST. Tube formation assay results indicated that 30 μM AST for 12 h was significantly improved HUVEC tube formation (Fig. S5a). Based on these findings, 30 μM AST for 12 h was chosen as the experimental condition for further study. HUVECs were divided into three groups: Control, HG (60 mM glucose for 48 h), and AST (60 mM glucose for 48 h, followed by 30 μM AST for 12 h). Scratch and Transwell migration assays demonstrated that HUVEC migration was significantly impaired in the HG group, while AST treatment restored migration ability compared to the HG group (Fig. 3e–f). Tube formation assays further revealed that AST significantly increased the number of tubes formed by HUVECs under HG conditions (Fig. 3g). Western blot analysis showed that AST markedly upregulated VEGF and CD31 expression in HUVECs, thereby enhancing angiogenesis *in vitro* (Fig. 3h).

In summary, these findings indicate that AST effectively induces M2 macrophage polarization, suppresses inflammation, and enhances angiogenesis in HUVECs, providing a promising therapeutic approach for diabetic wound healing.

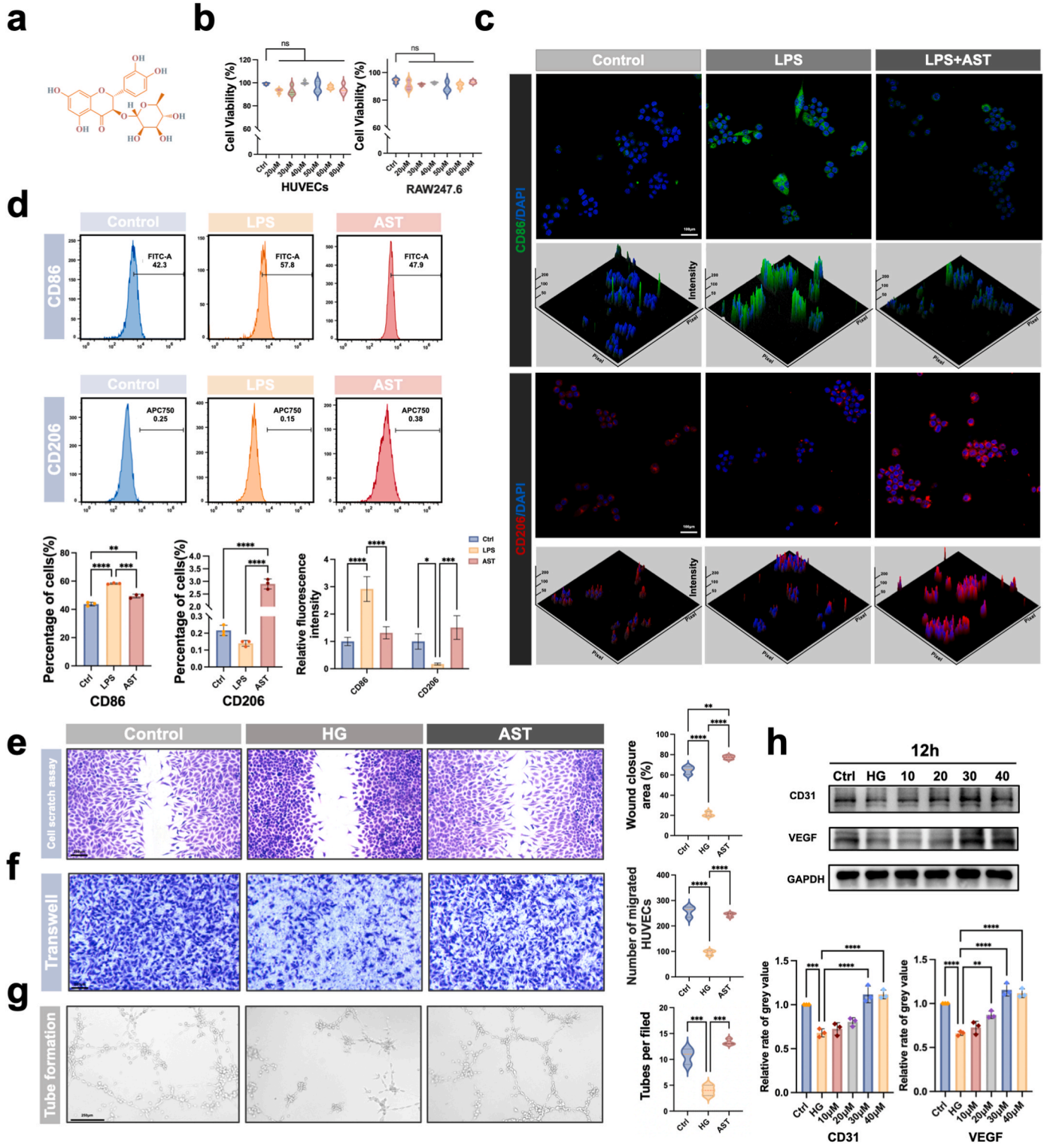

Fig. 3. Effects of AST on Macrophage Polarization and Angiogenesis in HUVECs. (a) Chemical structure of AST. (b) Cell viability assays of HUVECs and RAW264.7 macrophages treated with various concentrations of AST, showing no significant cytotoxicity. (c) Immunofluorescence staining of RAW264.7 macrophages for CD86 (M1 marker) and CD206 (M2 marker) under control, LPS, and LPS + AST conditions, demonstrating AST-induced M2 polarization. 3D intensity plots confirm increased CD206 expression with AST treatment. (d) Flow cytometry analysis of CD86 and CD206 expression in macrophages, showing a significant increase in M2 ($CD206^{+}$) and decrease in M1 ($CD86^{+}$) populations following AST treatment. (e) Scratch assay of HUVECs under high-glucose (HG) conditions with and without AST treatment, indicating enhanced wound closure with AST. (f) Transwell migration assay demonstrating increased HUVEC migration upon AST treatment. (g) Tube formation assay showing improved angiogenic capacity of HUVECs after AST treatment. (h) Western blot analysis of angiogenesis markers (CD31 and VEGF) in HUVECs, showing upregulated expression following AST treatment. The data are represented as mean ± SD (n = 3). *ns*: not significant, $^{*}P < 0.05$, $^{**}P < 0.01$, $^{***}P < 0.001$, $^{****}P < 0.0001$.

3.5. Mechanism of angiogenesis promotion by AST-loaded inner layer in HUVECs In vitro

To further explore the molecular mechanisms by which AST promotes angiogenesis in HUVECs under HG conditions, RNA-seq was conducted to evaluate changes in mRNA expression between the HG group and the AST-treated group (Fig. 4a). A total of 20,355 genes were identified, and the volcano plot indicated that numerous genes were significantly differentially expressed after 12 h of AST treatment (Fig. 4b). Cluster analysis revealed distinct gene expression patterns between the HG and AST groups (Fig. 4c).

Gene Set Enrichment Analysis (GSEA) indicated that the peroxisome pathway was significantly activated in the AST-treated group (Fig. 4d). Peroxisomes play a crucial role in ROS detoxification and maintaining cellular homeostasis. Western blot analysis revealed a significant upregulation of the peroxisomal membrane protein PEX3 in the AST-treated group, while PEX19 expression remained largely unchanged (Fig. 4f). Moreover, the results of *in vivo* immunohistochemical (IHC) analysis corroborated these findings, further supporting the observed trends (Fig. 4e). High-glucose conditions were observed to significantly suppress the expression of PEX3 and PEX19 (Fig. 4f), two critical proteins involved in peroxisome biogenesis. PEX3, which serves as a membrane anchor for peroxisomal membrane proteins (PMPs), exhibited a significant reduction in expression, potentially disrupting peroxisome biogenesis. Similarly, PEX19, a key mediator of PMP transport, also displayed decreased expression, further contributing to peroxisomal dysfunction. Notably, treatment with AST effectively restored PEX3 expression to near-normal levels, while PEX19 expression remained relatively unchanged. Based on the observed findings, it is hypothesized that AST exerts its effects by inhibiting pro-inflammatory pathways, including NF-κB, thereby reducing cytokine levels such as TNF-α, which are known to suppress PEX3 expression. Furthermore, AST may enhance fatty acid metabolism, thereby inducing a compensatory upregulation of PEX3 to meet the increased demand for peroxisomal β-oxidation. In contrast, the expression of PEX19 appears to remain intrinsically stable under oxidative stress, potentially due to its basal levels being sufficient to sustain PMP transport upon the restoration of PEX3 expression. Alternatively, PEX19 may be regulated through distinct signaling pathways that exhibit limited responsiveness to AST treatment [40,41,42].

Additionally, Gene Ontology (GO) analysis showed that the genes upregulated by AST were primarily enriched in functions related to cell adhesion, anchoring junctions, the cytoskeleton, and focal adhesions (Fig. 4h). Moreover, Kyoto Encyclopedia of Genes and Genomes (KEGG) pathway analysis identified significant changes in the actin cytoskeleton regulation pathway following AST treatment (Fig. 4k). To further assess the impact of AST on the cytoskeleton, phalloidin-rhodamine staining was performed. Fluorescence microscopy revealed that, as opposed to the control group, HUVECs in the HG group exhibited substantial cytoskeletal disruption, with noticeable breaks in F-actin fibers. In contrast, AST treatment protected the cells from these disruptions, promoting actin network reorganization and enhancing cell migration (Fig. 4g). Western blot analysis further illustrated that AST significantly upregulated the expression of RhoA, Cdc42 and Actin, key regulators of the cytoskeleton (Fig. 4j). Moreover, the results of *in vivo* IHC analysis corroborated these findings, further supporting the observed trends (Fig. 4i). Based on the findings, it is proposed that AST facilitates cell migration by promoting cytoskeletal remodeling. Specifically, AST may enhance actin polymerization at the leading edge, driving the formation of filopodia and lamellipodia, which are critical for initiating directional protrusions. Additionally, AST may regulate the organization of stress fibers and enhance actomyosin contractility, thereby increasing intracellular tension and enabling efficient trailing edge retraction. Moreover, AST might influence the coordinated interaction between actin filaments and microtubules, which is essential for maintaining cell polarity and directional persistence during migration. Collectively, these cytoskeletal modifications induced by AST likely optimize the biomechanical and dynamic properties necessary for enhanced cell motility [43,44,45]. The association between peroxisomes and the cytoskeleton, including microtubules and actin filaments, is a critical aspect of their dynamic functionality. This interaction involves multiple peroxisome-associated proteins that engage with motor proteins, adaptor proteins, or other cytoskeletal components [46]. However, whether AST can regulate cytoskeletal remodeling through peroxisomes remains unclear and will be further investigated in future experiments (Fig. 4l).

These findings collectively demonstrate that AST significantly improves HUVECs function under high-glucose conditions by restructuring the cytoskeleton and activating peroxisomes, thereby enhancing angiogenesis.

3.6. In Vivo ameliorate of diabetic wound healing by S/A@GelMN

The *in vitro* experiments confirmed that the outer layer of the S/A@GelMN system, containing Se-CQDs, exhibits potent antioxidant activity, while the inner layer, loaded with AST, induces M2 macrophage polarization and promotes angiogenesis. The efficacy of this system in promoting diabetic wound healing *in vivo* was subsequently evaluated.

Initially, we evaluated the *in vivo* biosafety of the S/AMN. Typical histopathological sections stained with H&E from the heart, liver, spleen, lung, and kidney of control group specimens, Se-CQDs@GleMN (SMN), AST@GleMN (AMN), and S/A @GelMN (S/AMN) groups after 14 days of administration showed no notable histopathological changes, such as inflammation, necrosis, or fibrosis, in any of the examined organs (Fig. S6a). These findings demonstrate the excellent biocompatibility and minimal systemic toxicity of the S/A@GelMN.

To assess the transdermal drug delivery performance of the S/A@GelMN system, Se-CQDs were labeled with Cy5.5, and two administration methods were compared: intradermal injection (ID group) and Se-CQDs@MN (MN group) (Fig. 5a–b). On the first day post-administration, both groups showed fluorescence in the dermal tissue, confirming successful drug release. However, in the MN group, there was a strong fluorescence signal concentrated at the wound site, indicating better local drug retention and controlled release. By day 4, the fluorescence in the ID group had nearly disappeared, while the MN group maintained a significant red fluorescence signal. *In vivo* imaging further confirmed that the MN group exhibited sustained fluorescence for up to 14 days, demonstrating the prolonged release of Se-CQDs by the S/A@GelMN system (Fig. 5a–c). Next, an *in vivo* study was conducted to explore the effective concentrations of Se-CQDs and AST loaded in the GleMN.

Diabetes was established in C57BL/6 mice through streptozotocin (STZ) administration, and the model was confirmed by fasting blood glucose levels exceeding 16.7 mmol/L. A full-thickness dorsal wound model was then created on the mice (Fig. 6a). Diabetic mice were randomly assigned to the following experimental groups: unloaded GleMN (Ctrl group), 500 μg/mL Se-CQDs (LS group), 1000 μg/mL Se-CQDs (HS group), 500 μM AST (LA group), and 1000 μM AST (HA group). Wound healing was monitored over 7 and 14 days, with results showing significant improvement in wound healing in the LS and HA groups (Fig. S7a). These findings confirmed that 1000 μg/mL Se-CQDs and 1000 μM AST were effective concentrations for promoting wound healing in diabetic mice.

With the optimal drug concentrations identified, diabetic mice were further divided into three treatment groups: Se-CQDs@GleMN (SMN), AST@GleMN (AMN), and S/A @GelMN (S/AMN), and wound healing was observed. Photographs of the wounds revealed that compared to the control group, all treatment groups (SMN, AMN, and S/AMN) exhibited significantly accelerated wound healing, with the S/AMN group showing the fastest healing, and nearly complete wound closure by day 14 (Fig. 6b). Histological analysis of wound tissues at day 14 using HE and Masson's trichrome staining, along with immunohistochemistry and

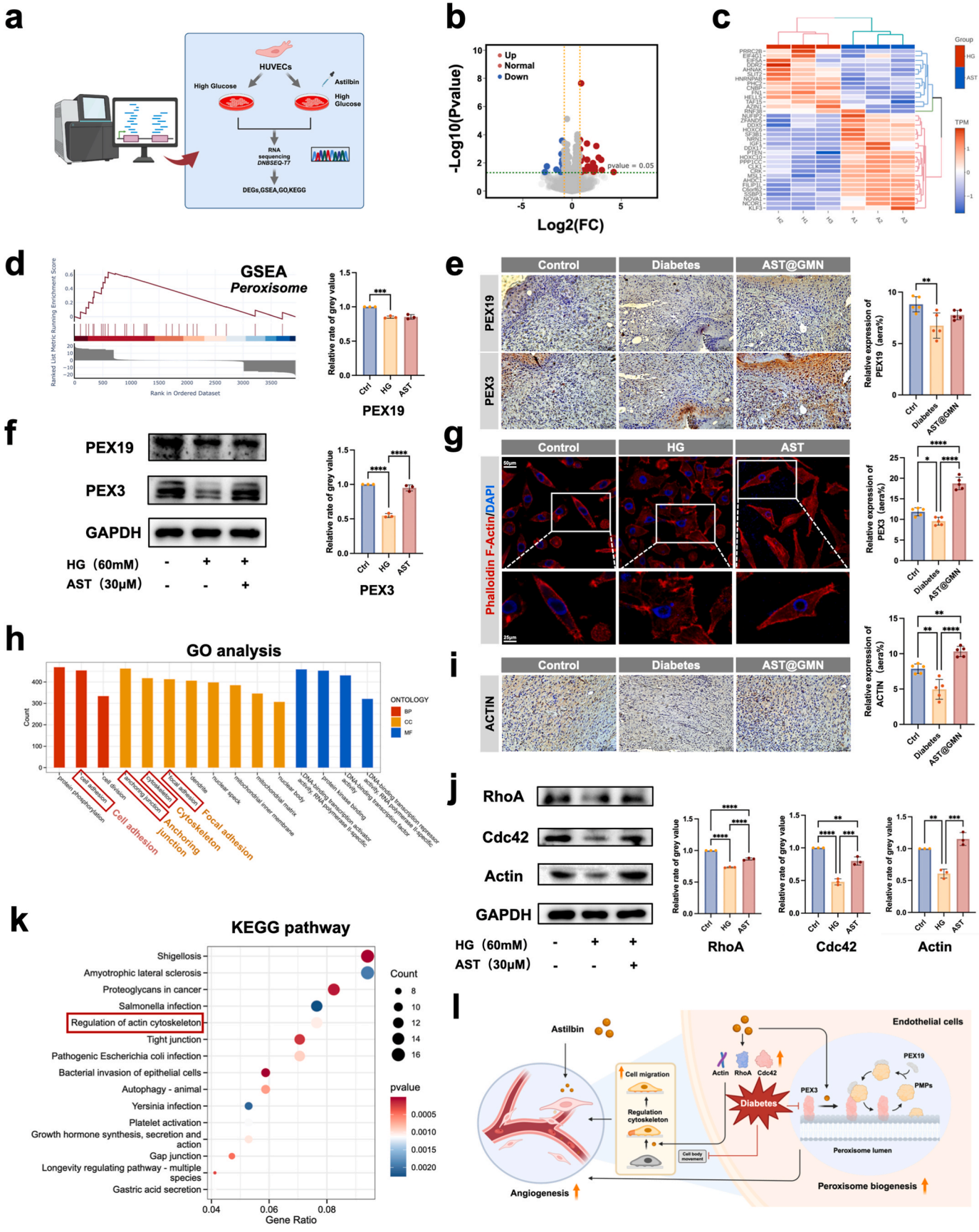

(caption on next page)

Fig. 4. AST promotes cytoskeletal remodeling and peroxisome function under high-glucose conditions. (a) Schematic of the experimental workflow for transcriptomic analysis of HUVECs treated with AST under high-glucose (HG) conditions, including RNA-seq, GSEA, and downstream validation. (b) Volcano plot showing differentially expressed genes (DEGs) between HG and AST-treated groups. Red and blue dots represent upregulated and downregulated genes, respectively. (c) Heatmap of hierarchical clustering illustrating distinct gene expression patterns between HG and AST-treated groups. (d) GSEA of the peroxisome pathway in AST-treated cells, showing significant enrichment. Relative mRNA levels of PEX3 and PEX19 were analyzed by RT-qPCR. (e) Representative immunohistochemistry (IHC) staining for PEX3 and PEX19 in wound tissue from Control, Diabetes, and AST@GelMN groups, with quantification of staining intensity. (f) Western blot analysis of PEX3 and PEX19 expression under HG conditions with or without AST treatment. (g) Phalloidin staining for F-actin showing cytoskeletal remodeling in Control, HG, and AST-treated cells. Quantification of F-actin intensity is provided.
(h) GO analysis of DEGs. (i) Representative IHC staining for Actin in wound tissues from Control, Diabetes, and AST@GelMN groups, with quantification of staining intensity. (j) Western blot analysis of RhoA, Cdc42, and Actin under HG conditions with or without AST treatment. Quantification of protein levels is shown. (k) KEGG pathway analysis of DEGs. (l) Schematic representation illustrating mechanism of AST. The data are represented as mean ± SD (n = 5). $^{**}P < 0.01$, $^{***}P < 0.001$, $^{****}P < 0.0001$. (For interpretation of the references to colour in this figure legend, the reader is referred to the Web version of this article.)

immunofluorescence at day 14, provided further insights into tissue repair. HE staining showed reduced wound area and decreased granulation tissue thickness in the S/AMN group (Fig. 6c). Masson's staining confirmed that collagen fibers in the S/AMN group were more densely packed and better aligned, indicating enhanced tissue remodeling and wound healing (Fig. 6d). Furthermore, CD31 IHC and IF staining demonstrated a significant increase in the number of CD31-positive vessels in the S/AMN group, indicating the system's effectiveness in promoting angiogenesis (Fig. 6e–f and S7b).

Moreover, the results of macrophage polarization staining underscore the robust immunomodulatory capabilities of the S/AMN in the diabetic wound model. The S/AMN-treated group exhibited a significant increase in CD206-positive M2 macrophages, indicative of an anti-inflammatory and tissue-regenerative phenotype, alongside a marked reduction in CD86-positive M1 macrophages, which are associated with pro-inflammatory responses. The transition from M1 to M2 macrophages underscores the immunomodulatory capacity of S/AMN within the wound microenvironment, shifting the immune environment from a pro-inflammatory toward a regenerative state (Fig. 7a–b). The observed immunomodulatory effects likely stem from the synergistic actions of Se-CQDs and AST, the active components of the dual-layer microneedles. Se-CQDs, loaded in the microneedle's outer layer, rapidly scavenge reactive ROS, thereby alleviating oxidative stress—a major driver of chronic inflammation and M1 macrophage activation. Concurrently, AST, encapsulated in the inner layer, is continuously released, contributing to the shift of macrophages toward an anti-inflammatory M2 phenotype. Inhibition of NF-κB signaling and increased IL-10 production may underlie this effect, which will be explored in future studies to clarify its mechanistic basis and therapeutic implications (Fig. 7c).

Our findings are in line with previous studies utilizing nanomaterial-based approaches for diabetic wound healing. For example, Hamed et al. reviewed diverse nanoparticles designed to address oxidative stress, infection, and inflammation in chronic wounds. Moreover, the use of multifunctional nanofiber dressings incorporating plant-derived ash demonstrated remarkable wound healing outcomes through modulation of wound pH and tissue microenvironment. Such evidence supports the promise of multifunctional and responsive systems, including our dual-loaded MNs, for future translation into diabetic wound management [47,48]. S/A@GelMN not only exhibits excellent therapeutic performance in the laboratory but also shows substantial potential for clinical applications. Firstly, the MN are non-invasive and user-friendly, overcoming the challenges of traditional wound dressings in penetrating skin barriers. MN can directly penetrate the skin, delivering drugs to subcutaneous lesions and significantly enhancing drug bioavailability [22]. Additionally, the convenience of MN allows patients to self-administer, improving compliance among diabetic patients and reducing hospitalization and medical costs. Furthermore, the controlled-release characteristics of the MN system offer the potential for long-term treatment. By adjusting the composition and manufacturing parameters of the MN, sustained drug release can be achieved, reducing the frequency of treatment for patients. This feature is particularly important for the treatment of chronic wounds. The successful application of S/A@GelMN in DW demonstrates its broad potential for personalized treatment in the future.

Compared with traditional transdermal delivery systems such as single-layer microneedles, nanocarriers, and hydrogel patches, the dual-layer S/A@GelMN offers enhanced precision and therapeutic efficacy. Single-layer microneedles lack programmable release, nanocarriers suffer from limited skin penetration, and hydrogel patches often fail to deliver drugs into deeper tissues. In contrast, S/A@GelMN combines mechanical penetration, sequential release, and microenvironment responsiveness, enabling rapid ROS clearance followed by sustained anti-inflammatory and pro-angiogenic effects. This integrated strategy effectively addresses multiple barriers to diabetic wound healing and shows superior performance in both *in vitro* and *in vivo* models [49,50,51,52]. To further enhance the applicability of the S/A@GelMN system, future designs could integrate stimuli-responsive elements to achieve intelligent, on-demand drug release. Incorporating pH or glucose-sensitive components may enable the microneedles to respond dynamically to pathological cues such as infection or inflammation [53,54,55]. Recent studies have demonstrated that microneedle patches equipped with biosensors or responsive hydrogels can detect abnormal wound microenvironments and trigger timely drug release accordingly [56,55,57]. This strategy may be adapted to optimize therapeutic precision and personalized wound care.

Despite the promising outcomes of S/A@GelMN in DW healing demonstrated in this study, several issues still require further exploration in future research. First, the long-term biocompatibility and potential toxicity of the MN system need thorough investigation, especially for frequent usage in patients. The safety of Se-CQDs should be assessed over extended observation periods and in broader models to ensure their safe and reliable application in humans. Additionally, different MN formulations may produce varying effects in different diabetic patients, indicating that personalized treatment remains a crucial direction for future research. Future studies should focus on optimizing the MN design and components based on individual patient pathological characteristics to develop more precise treatment regimens. Moreover, the stability and manufacturing process of S/A@GelMN need further investigation to ensure the feasibility of large-scale production for clinical application [24,6,58].

4. Conclusion

In this work, we successfully synthesized Se-CQDs and developed an innovative dual-layer GelMN system co-loaded with Se-CQDs and AST to address the complex therapeutic challenges associated with DW. Unlike conventional single-layer MNs, the dual-layer design enables the sequential release of therapeutic agents, leveraging the complementary effects of Se-CQDs and AST. The outer layer, enriched with Se-CQDs, provides rapid ROS scavenging, mitigating oxidative stress and minimizing cellular damage in hyperglycemic conditions. Subsequently, the inner layer facilitates the sustained release of AST, which exerts potent immunomodulatory and pro-angiogenic effects. Preliminary findings suggest that these effects may involve the regulation of cytoskeletal dynamics, peroxisome function, and macrophage polarization,

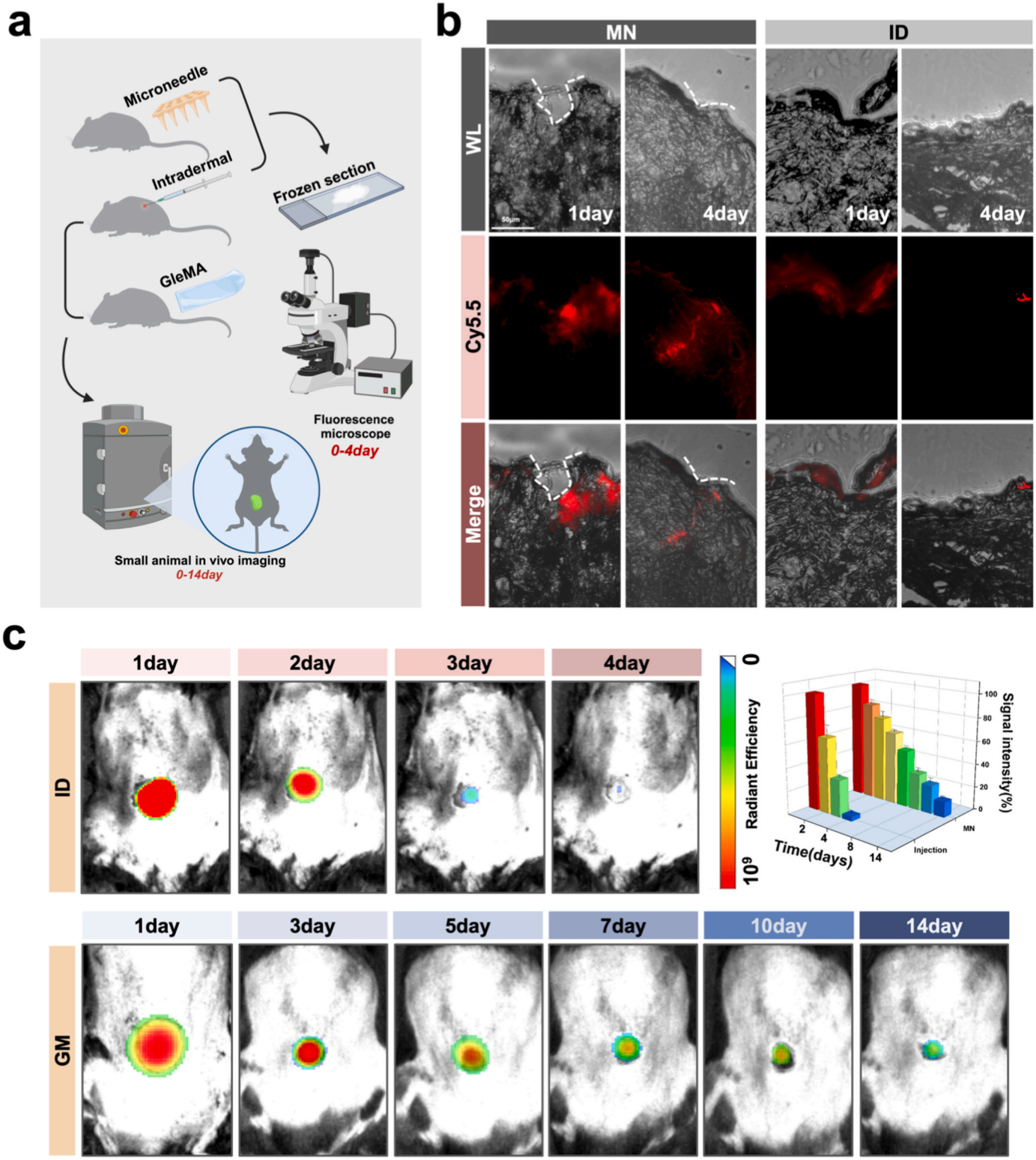

Fig. 5. In Vivo Penetration and Drug Retention of S/A@GelMN. (a) Schematic illustration of *in vivo* transdermal delivery and imaging process for Se-CQDs/AST@GelMN. (b) Fluorescence microscopy images comparing (MN) and intradermal injection (ID) administration. White light (WL) images and Cy5.5 fluorescence signal indicate better drug retention and localized delivery with the microneedle system at both 1 day and 4 days post-administration. (c) In vivo fluorescence imaging of mice over a 14-day period, comparing drug retention between ID injection and GelMN application.

collectively enhancing endothelial cell migration, immune modulation, and angiogenesis.

Comprehensive characterization and *in vitro* evaluations validated the strong ROS-scavenging capacity of Se-CQDs and the robust immunomodulatory and pro-angiogenic properties of AST. *In vivo* experiments further demonstrated the superior therapeutic efficacy of the S/A@GelMN system, with significant enhancements in wound closure, tissue remodeling, macrophage polarization, and neovascularization in

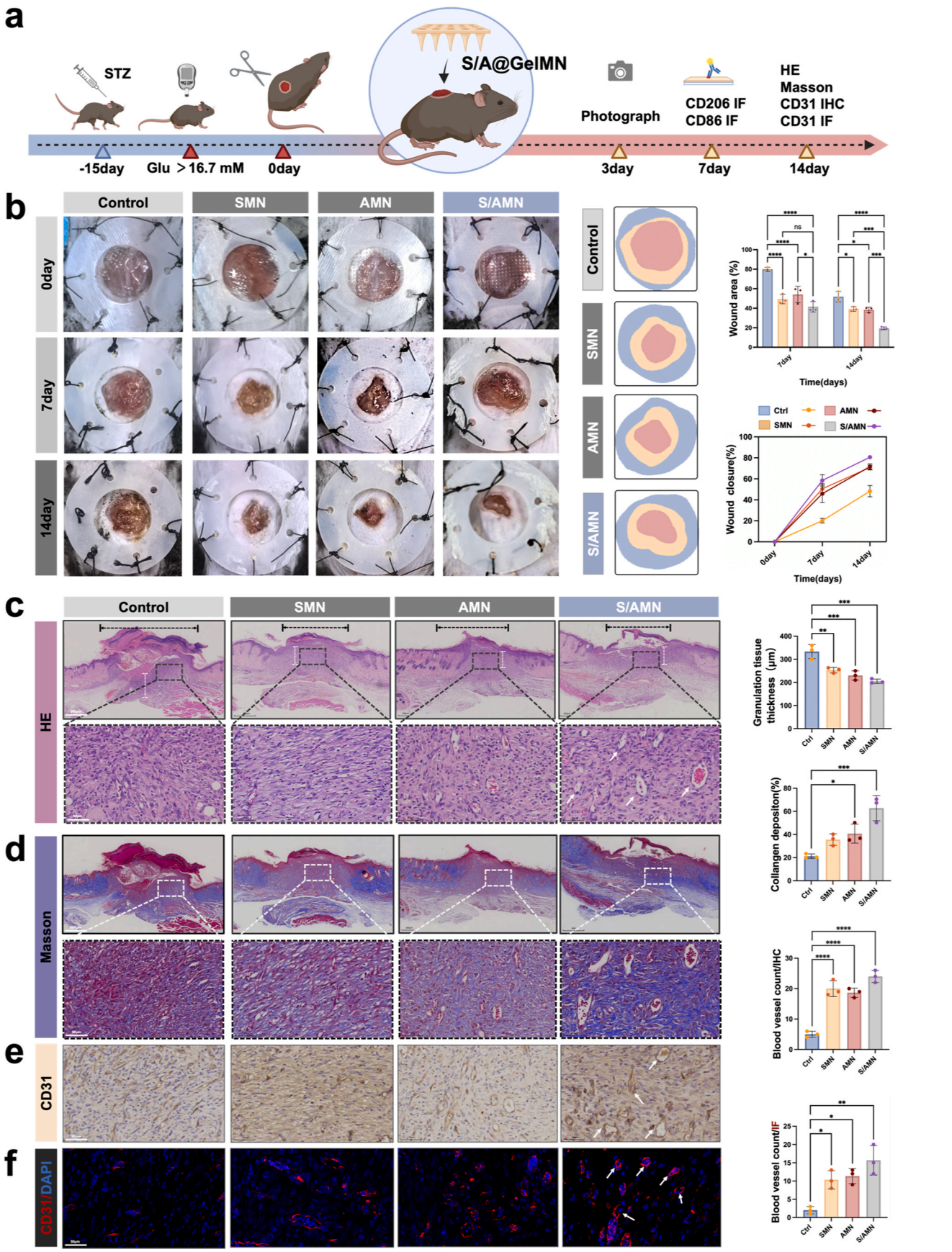

(caption on next page)

Fig. 6. In Vivo ameliorate of Diabetic Wound Healing by S/A@GelMN. (a) Schematic of the diabetic wound healing study design. Diabetic mice were induced using STZ, followed by full-thickness skin wound creation. The S/A@GelMN treatment was applied, with wound healing monitored at 3, 7, and 14 days using HE, Masson's trichrome staining, and CD31 IHC/IF analysis. (b) Representative wound images from Control, SMN, AMN, and S/AMN groups at day 0, 7, and 14, with quantitative analysis showing significantly enhanced wound closure in the S/AMN group. (c) HE staining at day 14 demonstrating improved granulation tissue thickness in the S/AMN group. Insets: Higher magnification images highlighting granulation. (d) Masson's trichrome staining at day 14 showing increased collagen deposition in the S/AMN-treated wounds. Insets: Enlarged views of collagen-rich regions. (e) CD31 IHC staining at day 14 indicating enhanced blood vessel formation in the S/AMN group. (f) CD31 IF staining at day 14 confirming a higher density of CD31-positive microvessels in the S/AMN-treated wounds. The data are represented as mean ± SD (n = 5). *ns*: not significant, $^{*}P < 0.05$, $^{**}P < 0.01$, $^{***}P < 0.001$, $^{****}P < 0.0001$.

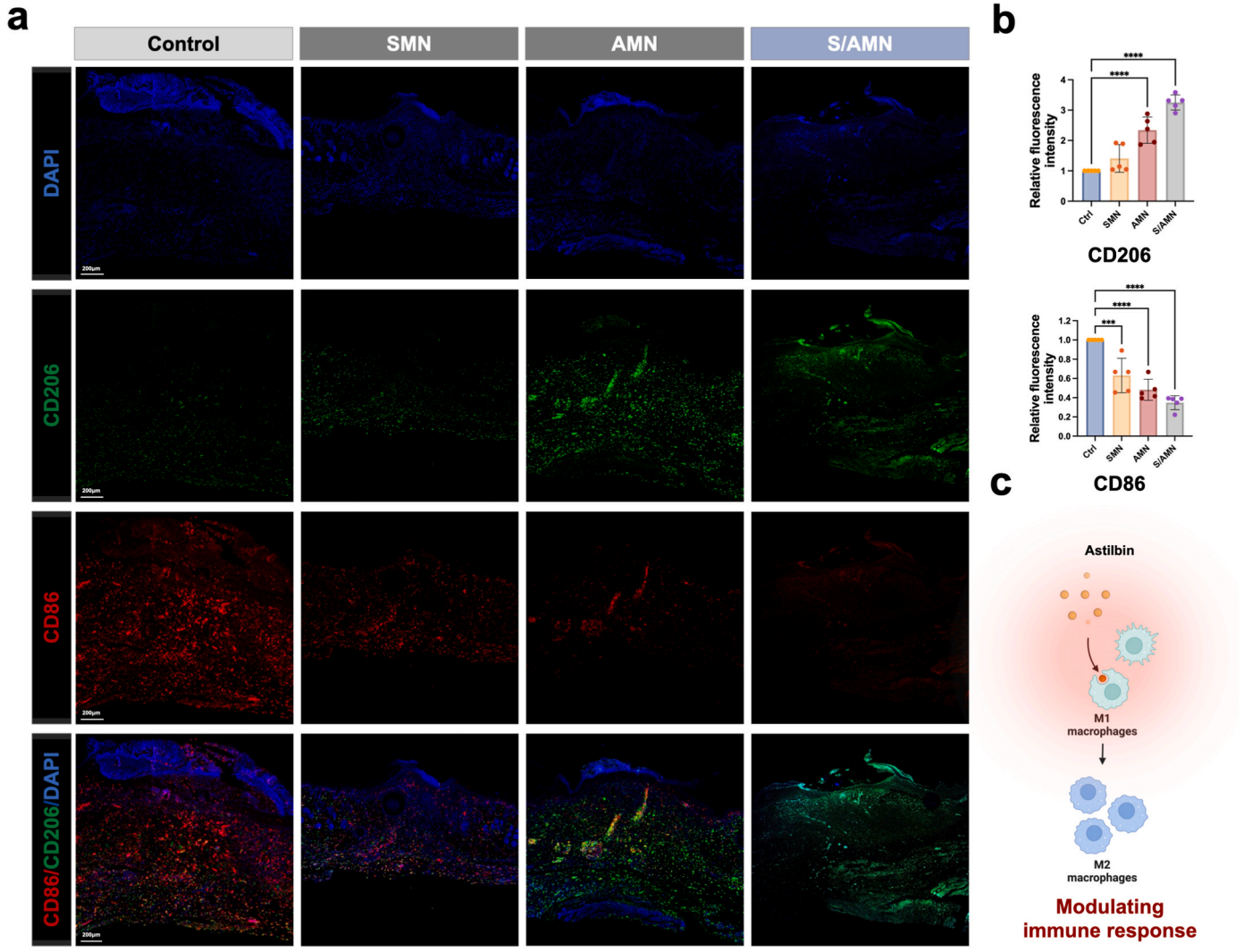

Fig. 7. Immunomodulatory effects of S/A@GelMN on macrophage polarization *in vivo*. (a) IF staining images for CD206 (M2 macrophage marker, green), CD86 (M1 macrophage marker, red), and DAPI (nuclei, blue) in wound tissues from the Control, SMN, AMN, and S/AMN groups. (b) Quantification of fluorescence intensity for CD206 and CD86 showing a significant increase in M2 macrophages and reduction in M1 macrophages in the S/AMN group. (c) Schematic representation illustrating the immunomodulatory mechanism of AST, promoting macrophage polarization from the pro-inflammatory M1 phenotype to the anti-inflammatory M2 phenotype, thereby modulating the immune response in the wound microenvironment. The data are represented as mean ± SD (n = 5). $^{***}P < 0.001$, $^{****}P < 0.0001$. (For interpretation of the references to colour in this figure legend, the reader is referred to the Web version of this article.)

diabetic mouse models, surpassing the performance of conventional drug delivery systems.

In conclusion, the successful synthesis of Se-CQDs and the development of the dual-layer GelMN system represent a novel and minimally invasive therapeutic strategy with substantial potential for personalized DW treatment. Future research should focus on evaluating the long-term biocompatibility of the system, optimizing formulations for patient-specific requirements, and scaling up production to facilitate clinical translation. In line with recent developments in smart wound dressings and nanomaterials, our approach contributes to the evolving field of multifunctional therapeutics. As evidenced by Cai et al. and Hamed et al., integrating physicochemical regulation (e.g., pH modulation, ROS control) with biological functionalities represents a promising direction for next-generation wound care. Therefore, future investigations should aim to refine our microneedle system to respond dynamically to the wound microenvironment, further enhancing its clinical translation potential [47,48,59].

CRediT authorship contribution statement

Zhen Zhang: Writing – review & editing, Writing – original draft, Resources, Project administration, Methodology, Data curation, Conceptualization. **Yulin Zhang:** Writing – review & editing, Writing – original draft, Formal analysis, Data curation. **Liang Peng:** Resources, Methodology, Data curation. **Yi Xing:** Formal analysis, Data curation. **Xinru Zhou:** Writing – review & editing, Writing – original draft, Data curation, Conceptualization. **Shuo Zheng:** Writing – review & editing, Formal analysis, Data curation. **Yanli Zhang:** Writing – review & editing, Supervision, Formal analysis, Data curation, Conceptualization. **Longquan Shao:** Writing – review & editing, Visualization, Funding acquisition, Conceptualization.

Declaration of competing interest

The authors declare that they have no known competing financial interests or personal relationships that could have appeared to influence the work reported in this paper.

Acknowledgements

This work was supported by the National Natural Science Foundation of China (82271025) and Science and Technology Projects in Guangzhou (202206010179). Some figures were generated using Biorender.

Appendix A. Supplementary data

Supplementary data to this article can be found online at https://doi.org/10.1016/j.mtbio.2025.101739.

Data availability

Data will be made available on request.

References

[1] N.H. Cho, J.E. Shaw, S. Karuranga, Y. Huang, J.D. da Rocha Fernandes, A. W. Ohlrogge, B. Malanda, IDF Diabetes Atlas: global estimates of diabetes prevalence for 2017 and projections for 2045, Diabetes Res. Clin. Pract. 138 (2018) 271–281, https://doi.org/10.1016/j.diabres.2018.02.023.

[2] D.G. Greenhalgh, Wound healing and diabetes mellitus, Clin. Plast. Surg. 30 (2003) 37–45, https://doi.org/10.1016/s0094-1298(02)00066-4.

[3] K. Ogurtsova, J.D. da Rocha Fernandes, Y. Huang, U. Linnenkamp, L. Guariguata, N.H. Cho, D. Cavan, J.E. Shaw, L.E. Makaroff, IDF Diabetes Atlas: global estimates for the prevalence of diabetes for 2015 and 2040, Diabetes Res. Clin. Pract. 128 (2017) 40–50, https://doi.org/10.1016/j.diabres.2017.03.024.

[4] J.E. Shaw, R.A. Sicree, P.Z. Zimmet, Global estimates of the prevalence of diabetes for 2010 and 2030, Diabetes Res. Clin. Pract. 87 (2010) 4–14, https://doi.org/10.1016/j.diabres.2009.10.007.

[5] D.G. Armstrong, T.W. Tan, A.J.M. Boulton, S.A. Bus, Diabetic foot ulcers: a review, JAMA 330 (2023) 62–75, https://doi.org/10.1001/jama.2023.10578.

[6] F. Huang, X. Lu, Y. Yang, Y. Yang, Y. Li, L. Kuai, B. Li, H. Dong, J. Shi, Microenvironment-based diabetic foot ulcer nanomedicine, Adv. Sci. (Weinh.) 10 (2023) e2203308, https://doi.org/10.1002/advs.202203308.

[7] G. Langer, C.S. Wan, A. Fink, L. Schwingshackl, D. Schoberer, Nutritional interventions for preventing and treating pressure ulcers, Cochrane Database Syst. Rev. 2 (2024) Cd003216, https://doi.org/10.1002/14651858.CD003216.pub3.

[8] S. Lin, Q. Wang, X. Huang, J. Feng, Y. Wang, T. Shao, X. Deng, Y. Cao, X. Chen, M. Zhou, C. Zhao, Wounds under diabetic milieu: the role of immune cellar components and signaling pathways, Biomed. Pharmacother. 157 (2023) 114052, https://doi.org/10.1016/j.biopha.2022.114052.

[9] U.A. Okonkwo, L.A. DiPietro, Diabetes and wound angiogenesis, Int. J. Mol. Sci. 18 (2017) 1419, https://doi.org/10.3390/ijms18071419.

[10] M. Sharifiaghdam, E. Shaabani, R. Faridi-Majidi, S.C. De Smedt, K. Braeckmans, J. C. Fraire, Macrophages as a therapeutic target to promote diabetic wound healing, Mol. Ther. 30 (2022) 2891–2908, https://doi.org/10.1016/j.ymthe.2022.07.016.

[11] Y. Xiong, X. Chu, T. Yu, S. Knoedler, A. Schroeter, L. Lu, K. Zha, Z. Lin, D. Jiang, Y. Rinkevich, A.C. Panayi, B. Mi, G. Liu, Y. Zhao, Reactive oxygen species-scavenging nanosystems in the treatment of diabetic wounds, Adv Healthc Mater 12 (2023) e2300779, https://doi.org/10.1002/adhm.202300779.

[12] Y. Chen, X. Wang, S. Tao, Q. Wang, P.Q. Ma, Z.B. Li, Y.L. Wu, D.W. Li, Research advances in smart responsive-hydrogel dressings with potential clinical diabetic wound healing properties, Mil Med Res 10 (2023) 37, https://doi.org/10.1186/s40779-023-00473-9.

[13] Y. Song, Y. You, X. Xu, J. Lu, X. Huang, J. Zhang, L. Zhu, J. Hu, X. Wu, X. Xu, W. Tan, Y. Du, Adipose-derived mesenchymal stem cell-derived exosomes biopotentiated extracellular matrix hydrogels accelerate diabetic wound healing and skin regeneration, Adv. Sci. (Weinh.) 10 (2023) e2304023, https://doi.org/10.1002/advs.202304023.

[14] J.R. Bardill, M.R. Laughter, M. Stager, K.W. Liechty, M.D. Krebs, C. Zgheib, Topical gel-based biomaterials for the treatment of diabetic foot ulcers, Acta Biomater. 138 (2022) 73–91, https://doi.org/10.1016/j.actbio.2021.10.045.

[15] D. Dayya, O.J. O'Neill, T.B. Huedo-Medina, N. Habib, J. Moore, K. Iyer, Debridement of diabetic foot ulcers, Adv. Wound Care 11 (2022) 666–686, https://doi.org/10.1089/wound.2021.0016.

[16] T. Xiang, Q. Guo, L. Jia, T. Yin, W. Huang, X. Zhang, S. Zhou, Multifunctional hydrogels for the healing of diabetic wounds, Adv Healthc Mater 13 (2024) e2301885, https://doi.org/10.1002/adhm.202301885.

[17] P. Jiang, Q. Li, Y. Luo, F. Luo, Q. Che, Z. Lu, S. Yang, Y. Yang, X. Chen, Y. Cai, Current status and progress in research on dressing management for diabetic foot ulcer, Front. Endocrinol. 14 (2023) 1221705, https://doi.org/10.3389/fendo.2023.1221705.

[18] S. Lyu, Z. Dong, X. Xu, H.P. Bei, H.Y. Yuen, C.W. James Cheung, M.S. Wong, Y. He, X. Zhao, Going below and beyond the surface: microneedle structure, materials, drugs, fabrication, and applications for wound healing and tissue regeneration, Bioact. Mater. 27 (2023) 303–326, https://doi.org/10.1016/j.bioactmat.2023.04.003.

[19] J. Pei, C.P. Palanisamy, P. Alugoju, N.V.A. Anthikapalli, P.M. Natarajan, V. R. Umapathy, B. Swamikannu, S. Jayaraman, P. Rajagopal, S. Poompradub, A comprehensive review on bio-based materials for chronic diabetic wounds, Molecules 28 (2023) 604, https://doi.org/10.3390/molecules28020604.

[20] W.X. Li, X.P. Zhang, B.Z. Chen, W.M. Fei, Y. Cui, C.Y. Zhang, X.D. Guo, An update on microneedle-based systems for diabetes, Drug Deliv Transl Res 12 (2022) 2275–2286, https://doi.org/10.1007/s13346-021-01113-2.

[21] F. Qu, R. Geng, Y. Liu, J. Zhu, Advanced nanocarrier- and microneedle-based transdermal drug delivery strategies for skin diseases treatment, Theranostics 12 (2022) 3372–3406, https://doi.org/10.7150/thno.69999.

[22] D. Yang, M. Chen, Y. Sun, Y. Jin, C. Lu, X. Pan, G. Quan, C. Wu, Microneedle-mediated transdermal drug delivery for treating diverse skin diseases, Acta Biomater. 121 (2021) 119–133, https://doi.org/10.1016/j.actbio.2020.12.004.

[23] H. Li, J. Li, J. Xu, L. Li, Y. Wang, C. Liu, J. Zhou, Advances in dermatological application of GelMA hydrogel microneedles, Skin Res. Technol. 29 (2023) e13327, https://doi.org/10.1111/srt.13327.

[24] J. Gan, X. Zhang, W. Ma, Y. Zhao, L. Sun, Antibacterial, adhesive, and MSC exosomes encapsulated microneedles with spatio-temporal variation functions for diabetic wound healing, Nano Today 47 (2022) 101630, https://doi.org/10.1016/j.nantod.2022.101630.

[25] Y. Meng, X.J. Li, Y. Li, T.Y. Zhang, D. Liu, Y.Q. Wu, F.F. Hou, L. Ye, C.J. Wu, X. D. Feng, X.J. Ju, L. Jiang, Novel double-layer dissolving microneedles for transmucosal sequential delivery of multiple drugs in the treatment of oral mucosa diseases, ACS Appl. Mater. Interfaces 15 (2023) 13892–13906, https://doi.org/10.1021/acsami.2c19913.

[26] Y. Yu, Y. Gao, Y. Zeng, W. Ge, C. Tang, X. Xie, L. Liu, Multifunctional hyaluronic acid/gelatin methacryloyl core-shell microneedle for comprehensively treating oral mucosal ulcers, Int. J. Biol. Macromol. 266 (2024) 131221, https://doi.org/10.1016/j.ijbiomac.2024.131221.

[27] H. Diao, Z. Kang, F. Han, W. Jiang, Astilbin protects diabetic rat heart against ischemia-reperfusion injury via blockade of HMGB1-dependent NF-κB signaling pathway, Food Chem. Toxicol. 63 (2014) 104–110, https://doi.org/10.1016/j.fct.2013.10.045.

[28] G.S. Li, W.L. Jiang, X.D. Yue, G.W. Qu, J.W. Tian, J. Wu, F.H. Fu, Effect of astilbin on experimental diabetic nephropathy *in vivo* and *in vitro*, Planta Med. 75 (2009) 1470–1475, https://doi.org/10.1055/s-0029-1185802.

[29] M. Sumiyoshi, Y. Kimura, Enhancing effects of a chromone glycoside, eucryphin, isolated from Astilbe rhizomes on burn wound repair and its mechanism, Phytomedicine 17 (2010) 820–829, https://doi.org/10.1016/j.phymed.2010.01.010.

[30] F. Chen, Z. Sun, X. Zhu, Y. Ma, Astilbin inhibits high glucose-induced autophagy and apoptosis through the PI3K/Akt pathway in human proximal tubular epithelial cells, Biomed. Pharmacother. 106 (2018) 1175–1181, https://doi.org/10.1016/j.biopha.2018.07.072.

[31] F. Li, T. Li, C. Sun, J. Xia, Y. Jiao, H. Xu, Selenium-doped carbon quantum dots for free-radical scavenging, Angew Chem Int Ed Engl. 56 (2017) 9910–9914, https://doi.org/10.1002/anie.201705989.

[32] Z.T. Rosenkrans, T. Sun, D. Jiang, W. Chen, T.E. Barnhart, Z. Zhang, C.A. Ferreira, X. Wang, J.W. Engle, P. Huang, W. Cai, Selenium-doped carbon quantum dots act as broad-spectrum antioxidants for acute kidney injury management, Adv. Sci. (Weinh.) 7 (2020) 2000420, https://doi.org/10.1002/advs.202000420.

[33] Y. Cao, B. Chen, Q. Liu, Y. Mao, Y. He, X. Liu, X. Zhao, Y. Chen, X. Li, Y. Li, L. Liu, C. Guo, S. Liu, F. Tan, H. Lu, J. Liu, C. Chen, Dissolvable microneedle-based wound dressing transdermally and continuously delivers anti-inflammatory and pro-angiogenic exosomes for diabetic wound treatment, Bioact. Mater. 42 (2024) 32–51, https://doi.org/10.1016/j.bioactmat.2024.08.016.

[34] B. Bai, S. Qi, K. Yang, X. Yu, R. Jian, T. Zhang, D. Wang, H. Meng, Y. Zhao, Y. Xia, H. Xu, G. Yu, Z. Chen, Self-assembly of selenium-doped carbon quantum dots as antioxidants for hepatic ischemia-reperfusion injury management, Small 19 (2023) e2300217, https://doi.org/10.1002/smll.202300217.

[35] H. Wang, S. Sun, Y. Zhao, P. Wang, Y. Zhou, H. Sun, J. Yang, K. Cheng, S. Li, H. Lin, Carbon dots with integrated photothermal antibacterial and heat-enhanced

antioxidant properties for diabetic wound healing, Small (2024) 2403160, https://doi.org/10.1002/smll.202403160.
[36] Y. Liu, G. Xia, Y. Chen, H. Xia, J. Xu, L. Guo, S. Lin, Y. Liu, Purpurolide C-based microneedle promotes macrophage-mediated diabetic wound healing via inhibiting TLR4-MD2 dimerization and MYD88 phosphorylation, Acta Pharm. Sin. B 13 (2023) 5060–5073, https://doi.org/10.1016/j.apsb.2023.05.032.
[37] Q. Meng, E. Xie, H. Sun, H. Wang, J. Li, Z. Liu, K. Li, J. Hu, Q. Chen, C. Liu, B. Li, F. Han, High-strength smart microneedles with "offensive and defensive" effects for intervertebral disc repair, Adv Mater. 36 (2024) e2305468, https://doi.org/10.1002/adma.202305468.
[38] Z.-R. Yang, H. Suo, J.-W. Fan, N. Lv, K. Du, T. Ma, H. Qin, Y. Li, L. Yang, N. Zhou, Endogenous stimuli-responsive separating microneedles to inhibit hypertrophic scar through remodeling the pathological microenvironment, Nat. Commun. 15 (2024) 2038, https://doi.org/10.1038/s41467-024-46328-2.
[39] S.M. Baumgartner-Parzer, L. Wagner, M. Pettermann, J. Grillari, A. Gessl, W. Waldhäusl, High-glucose–triggered apoptosis in cultured endothelial cells, Diabetes 44 (1995) 1323–1327, https://doi.org/10.2337/diab.44.11.1323.
[40] R.L.M. Jansen, C. Santana-Molina, M. van den Noort, D.P. Devos, I.J. van der Klei, Comparative genomics of peroxisome biogenesis proteins: making sense of the PEX proteins, Front. Cell Dev. Biol. 9 (2021) 654163, https://doi.org/10.3389/fcell.2021.654163.
[41] J.T. Sun, Z.M. Wang, L.H. Zhou, T.T. Yang, D. Zhao, Y.L. Bao, S.B. Wang, L.F. Gu, J. W. Chen, T.K. Shan, T.W. Wei, H. Wang, Q.M. Wang, X.Q. Kong, L.P. Xie, A.H. Gu, Y. Zhao, F. Chen, Y. Ji, Y.Q. Cui, L.S. Wang, PEX3 promotes regenerative repair after myocardial injury in mice through facilitating plasma membrane localization of ITGB3, Commun. Biol. 7 (2024) 795, https://doi.org/10.1038/s42003-024-06483-0.
[42] K.M. Zientara-Rytter, S.S. Mahalingam, J.C. Farré, K. Carolino, S. Subramani, Recognition and chaperoning by Pex19, followed by trafficking and membrane insertion of the peroxisome proliferation protein, Pex11, Cells 11 (2022) 157, https://doi.org/10.3390/cells11010157.
[43] H. Ryu, H.N. Lee, J. Ju, J.-B. Park, E. Oh, M.Z. Lin, J. Seong, Combinatorial effects of RhoA and Cdc42 on the actin cytoskeleton revealed by photoswitchable GEFs, Sensor. Actuator. B Chem. 369 (2022) 132316, https://doi.org/10.1016/j.snb.2022.132316.
[44] N. Tapon, A. Hall, Rho, Rac and Cdc42 GTPases regulate the organization of the actin cytoskeleton, Curr. Opin. Cell Biol. 9 (1997) 86–92, https://doi.org/10.1016/s0955-0674(97)80156-1.
[45] S. Zhang, Y. Yin, C. Li, Y. Zhao, Q. Wang, X. Zhang, PAK4 suppresses TNF-induced release of endothelial microparticles in HUVECs cells, Aging (Albany NY) 12 (2020) 12740–12749, https://doi.org/10.18632/aging.103173.
[46] L. Schollenberger, T. Gronemeyer, C.M. Huber, D. Lay, S. Wiese, H.E. Meyer, B. Warscheid, R. Saffrich, J. Peränen, K. Gorgas, W.W. Just, RhoA regulates peroxisome association to microtubules and the actin cytoskeleton, PLoS One 5 (2010) e13886, https://doi.org/10.1371/journal.pone.0013886.
[47] Y. Cai, Z. Liao, Z. Xue, Z. Xue, J. Mei, L. Zhou, G. Zhang, W. Gan, Plant ash/polylactic acid electrospun fiber dressing promotes wound healing through pH regulation, Nano Biomed. Eng. 16 (2024) 588, https://doi.org/10.26599/NBE.2024.9290108.
[48] S.H. Hamed, E.A. Azooz, E.A.J. Al-Mulla, Nanoparticles-assisted wound healing: a review, Nano Biomed. Eng. 15 (2023) 425–435, https://doi.org/10.26599/NBE.2023.9290039.
[49] L. Barnum, J. Quint, H. Derakhshandeh, M. Samandari, F. Aghabaglou, A. Farzin, L. Abbasi, S. Bencherif, A. Memic, P. Mostafalu, 3D-printed hydrogel-filled microneedle arrays, Adv. Healthcare Mater. 10 (2021) 2001922, https://doi.org/10.1002/adhm.202001922.
[50] A. Golshirazi, M. Mohammadzadeh, S. Labbaf, The synergistic potential of hydrogel microneedles and nanomaterials: breaking barriers in transdermal therapy, Macromol. Biosci. 25 (2025) 2400228, https://doi.org/10.1002/mabi.202400228.
[51] P. Khairnar, V. Phatale, S. Shukla, A.O. Tijani, A. Hedaoo, J. Strauss, G. Verana, G. Vambhurkar, A. Puri, S. Srivastava, Nanocarrier-integrated microneedles: divulging the potential of novel frontiers for fostering the management of skin ailments, Mol. Pharm. 21 (2024) 2118–2147, https://doi.org/10.1021/acs.molpharmaceut.4c00144.
[52] Y. Zeng, C. Wang, J. Lei, X. Jiang, K. Lei, Y. Jin, T. Hao, W. Zhang, J. Huang, W. Li, Spatiotemporally responsive cascade bilayer microneedles integrating local glucose depletion and sustained nitric oxide release for accelerated diabetic wound healing, Acta Pharm. Sin. B 14 (2024) 5037–5052, https://doi.org/10.1016/j.apsb.2024.06.014.
[53] M. Liu, J. You, Y. Zhang, L. Zhang, S. Quni, H. Wang, Y. Zhou, Glucose-responsive self-healing bilayer drug microneedles promote diabetic wound healing via a Trojan-horse strategy, ACS Appl. Mater. Interfaces 16 (2024) 24351–24371, https://doi.org/10.1021/acsami.4c03050.
[54] X. Peng, Q. Peng, M. Wu, W. Wang, Y. Gao, X. Liu, Y. Sun, D. Yang, Q. Peng, T. Wang, A pH and temperature dual-responsive microgel-embedded, adhesive, and tough hydrogel for drug delivery and wound healing, ACS Appl. Mater. Interfaces 15 (2023) 19560–19573, https://doi.org/10.1021/acsami.2c21255.
[55] Y. Wang, B. Gao, B. He, Toward efficient wound management: bioinspired microfluidic and microneedle patch, Small 19 (2023) 2206270, https://doi.org/10.1002/smll.202206270.
[56] H. Li, B. Li, D. Lv, W. Li, Y. Lu, G. Luo, Biomaterials releasing drug responsively to promote wound healing via regulation of pathological microenvironment, Adv. Drug Deliv. Rev. 196 (2023) 114778, https://doi.org/10.1016/j.addr.2023.114778.
[57] W. Zhang, J. Hu, H. Wu, X. Lin, L. Cai, Stimuli-responsive hydrogel dressing for wound healing, APL Mater. 13 (2025) 010601, https://doi.org/10.1063/5.0245545.
[58] L. Ou, B. Song, H. Liang, J. Liu, X. Feng, B. Deng, T. Sun, L. Shao, Toxicity of graphene-family nanoparticles: a general review of the origins and mechanisms, Part. Fibre Toxicol. 13 (2016) 1–24, https://doi.org/10.1186/s12989-016-0168-y.
[59] L. Wang, C. Hu, L. Shao, The antimicrobial activity of nanoparticles: present situation and prospects for the future, Int. J. Nanomed. (2017) 1227–1249, https://doi.org/10.2147/IJN.S121956.